



Graphite Particle-Size Induced Morphological and Performance Changes of Graphite–Silicon Electrodes

Fabian Jeschull,¹ Yuri Surace,¹ Simone Zürcher,² Giacomo Lari,² Michael E. Spahr,² Petr Novák,¹ and Sigita Trabesinger^{1,*}

¹*Electrochemistry Laboratory, 5232 Villigen PSI, Switzerland*

²*Imerys Graphite & Carbon, 6804 Bironico, Switzerland*

Silicon is a long-standing candidate for replacing graphite as the active material in negative electrodes for Li-ion batteries, due to its significantly higher specific capacity. However, Si suffers from rapid capacity fading, as a result of the large volume expansion upon lithiation. As an alternative to pure Si electrodes, Si could be used, instead, as a capacity-enhancing additive in graphite electrodes. Such graphite–Si blended electrodes exhibit lower irreversible-charge losses during the formation of the passivation layer and maintain a better electronic contact than pure Si electrodes. While previous works have mostly focused on the Si properties and Si content, this study investigates how the choice of graphite matrix can alter the electrode properties. By varying the type of graphite and the Si content (5 or 20 wt%), different electrode morphologies were obtained and their capacity retention upon long-term cycling was studied. Despite unfavorable electrode morphologies, such as large void spaces and poor active-material distribution, certain types of graphites with large particle sizes were found to be competitive with graphite–Si blends, containing smaller graphite particles. In an attempt to mitigate excess void-space and inhomogeneous material distribution, two approaches were examined: densification (calendering) and blending in a fraction of smaller graphite particles. While the former approach led in general to poorer capacity retention, the latter yielded an improved Coulombic efficiency without compromising the cycling performance.

© 2020 The Author(s). Published on behalf of The Electrochemical Society by IOP Publishing Limited. This is an open access article distributed under the terms of the Creative Commons Attribution 4.0 License ([CC BY](http://creativecommons.org/licenses/by/4.0/), <http://creativecommons.org/licenses/by/4.0/>), which permits unrestricted reuse of the work in any medium, provided the original work is properly cited. [DOI: [10.1149/1945-7111/ab9b9a](https://doi.org/10.1149/1945-7111/ab9b9a)]



Manuscript submitted January 5, 2020; revised manuscript received May 29, 2020. Published June 18, 2020.

Supplementary material for this article is available [online](#)

In the pursuit of ever higher energy densities for lithium-ion batteries (LIB), each component in the cell has to be continuously evaluated and optimized. Even if the largest improvements are expected from new positive-electrode materials with higher operating potentials and higher capacities, substantial improvements are possible on the negative-electrode side as well.¹ An obvious parameter is the electrode capacity, which can be improved by substituting the standard active material, graphite, partly or fully with alternative materials, possessing higher specific charge, for instance Si,^{2–6} Sn⁷ or SnO₂.⁸ However, while the theoretical specific charge of these materials is promising, they generally lack stability in terms of capacity retention when used in their pure form.⁹ Therefore, a partial substitution of graphite seems to be more realistic and, according to recent energy-density estimations,¹⁰ sufficient to significantly increase the energy density of state-of-the-art batteries on the cell level.

Blends of graphite and Si offer a good compromise between the inherently unstable Si^{11,12} and the reliable graphite electrode.^{13–15} The specific charge can theoretically range from 372 mAh g⁻¹ (100% graphite) to 3578 mAh g⁻¹ (100% Si; Li₁₅Si₄), and can be tuned to be optimal for the targeted application. Even small amounts of Si can increase the electrode capacity considerably (e.g., 5 wt% Si increase the capacity by approx. 170 mAh g⁻¹). We note that compared to other “Si/C” or “Si/Gr” composite electrodes⁶ that are reported in literature, the active material mixtures discussed here are blends of graphite and Si powders (referred to as graphite–Si blends in the following) and are used without further modification.

The addition of Si is associated with the usual problems of unstable interfaces^{16–19} and loss of electrical contact^{20,21} due to the substantial volume changes of Si during the alloying reaction.²² By keeping the Si content low, the volume expansion can be buffered largely by the void space between the much larger graphite particles.²³ Unlike neat Si electrodes, which require rather large amounts of conductive additive, the electrical conductivity of these

graphite electrodes with low Si contents is improved drastically due to the large fraction of graphite particles, as is obvious from the reduced voltage hysteresis.¹⁵ Nonetheless, in the presence of Si the issue of an unstable electrode–electrolyte interface remains. As a consequence, considerable consumption of the electrolyte additive fluoroethylene carbonate (FEC) has been observed in several studies.^{8,24–26}

We have recently investigated the impact of the Si content in these electrodes on cycle life, using 5–20 wt% Si.¹⁵ In this previous study, small graphite particles ($d_{90} < 6.9 \mu\text{m}$) were used, which overall led to a good dispersion as long as the Si content remained below 10 wt%. Graphites of small particle size are commonly used as conductive additives in battery electrodes, in addition to carbon blacks, and are typically not the main active material.²⁷ For the negative electrode this is motivated by the higher surface area of smaller particles, which inevitably results in larger irreversible losses during SEI formation.^{28,29} Despite its particle size and particle-size distribution, each sort of graphite thus comes with a unique set of physical properties that need to be taken into account, when selecting the active material for a graphite–Si blend.³⁰ Several previous works have demonstrated that the morphology of graphite–Si electrodes is greatly affected by the Si content.^{15,23,31}

Therefore, the aim of the present study is to investigate the impact of different types of graphites on the electrochemical performance of graphite–Si electrodes. Our test matrix comprises electrode formulations with four different kinds of graphite and two different Si contents (5 wt% & 20 wt%). We will show how different graphite properties result in different cycling behavior and how the particle size affects electrode morphology and performance.

Experimental

Materials.—All materials were used as received, unless stated otherwise. The graphites KS6L, SFG6L, SFG44 and Actilon1, as well as the conductive additive Super C45, were provided by Imerys Graphite & Carbon (Bodio, Switzerland). Silicon nanoparticles (30–50 nm) were purchased from Nanostructured & Amorphous Materials Inc. (Houston, USA). A binder mixture, containing carboxymethylcellulose sodium salt (CMC-Na, Alfa Aesar) and

*Electrochemical Society Member.

[†]E-mail: sigita.trabesinger@psi.ch

polyacrylic acid (PAA, 25 wt% aqueous solution, $M_w = 240,000$, Aldrich), was used in all electrode formulations. Circular electrodes with 13-mm diameter were punched out of a lithium foil (99.9%, 700 μm , Alfa Aesar) and stored in an Ar-filled glovebox. Nonwoven glass-fiber separators (EUJ 116, Hollingsworth & Vose, UK) were dried overnight at 120 °C under vacuum before being placed in a glovebox. The electrolyte in this study was a solution of 1 M LiPF₆ in ethylene carbonate (EC) and dimethylcarbonate (DMC) (v/v = 1:1) (LP30, BASF) and 4 wt% of fluoroethylene carbonate (FEC, BASF).

Electrode preparation.—Electrode slurries were prepared in batches of 2 g (for each KS6L and SFG6L) and 3 g (for SFG44 and Actilion 1), respectively. The electrode components (for details, see Table I) were gradually added to a 10-ml vial and mixed using an ultra turrax (IKA Ultra Turrax T25), set to a speed between 15,000 and 16,000 rpm.

Electrode preparation with a CMC-Na:PAA (1:1) binder mixture.—CMC-Na (2 wt%) and PAA (2 wt%) were first added to 1.5 g of an water:ethanol mixture (w/w = 70:30) until the CMC-Na powder was completely dissolved. Then carbon black (1 wt%) was added and blended with the binder solution for 2 min. In the next step, silicon nanopowder (5–20 wt%) with additional 1–1.5 g of the water:ethanol solution was added. The slurry was homogenized for another 2 min. Lastly, graphite (75–90 wt%) was added in two batches together with 0.5–1 g of the water:ethanol solution and stirred for 2 min after each addition. Adjustments to the slurry viscosity were made by adding small quantities (<300 μl) of the water:ethanol solution and mixing for another minute. For reference measurements, graphite electrodes containing no silicon were also prepared, following the general procedure described above. The slurries were left to degas for at least 30 min before they were cast onto Cu-foil (22- μm thickness, Schlenk Metalfolien, Germany). The coating was dried briefly under ambient conditions and then treated at 150 °C under reduced pressure for 2 h. The electrodes were then cut into circular discs of 13-mm diameter and then further dried overnight in the glovebox antechamber in vacuum at 120 °C.

Calendering electrodes.—The calender (Siemens) was operated at a roll temperature of 40 °C. The gap between roll and substrate was decreased from 100 μm to 60 μm in three steps. The sample thickness was checked after each step. The roll was pressurized to 4 bar with compressed air (higher pressures of up to 7 bar did not yield higher densities).

Cell assembly and electrochemical tests.—**Cell assembly.**—All potentials are referred vs Li⁺/Li. Two-electrode half-cells were assembled in an in-house coin-type cell design.³² The three glass-fiber separators, soaked with 500 μl of electrolyte (LP30 + 4 wt% FEC), were sandwiched between the electrodes. The cells were then closed with a constant torque of 15 Nm using a torque wrench.

Cell cycling in half-cells.—Regular cell cycling was carried out with an Astrol battery cycler (Astrol Electronics AG, Switzerland) in a temperature-controlled environment at 25 °C. The graphite–Si electrodes were cycled between 0.005 and 1.5 V. A conditioning cycle was carried out prior to the actual cycling test. In the first cycle, a rate of C/25 was applied for both lithiation and delithiation. The constant current (CC) cycling was followed by a constant potential (CP) step. The potential was held at the cut-off potential until the current dropped below C/50. In subsequent cycles, the lithiation of the working electrode was carried out at C/10 with a current cut-off in the CP-step of C/20; for delithiation, a rate of C/3 was applied with a current-off of C/20 in the CP-step.

SEM cross-section analysis.—Pristine electrodes were prepared by ion-milling the samples for 4 h in a Hitachi IM4000plus device at an acceleration voltage of 4 kV (ion current approx. 120 μA). For

morphological analysis, the sample was transferred into a scanning electron microscope (SEM, Zeiss Gemini). Electron micrographs were recorded at an acceleration voltage of 5 kV with both the in-lens and secondary electron detectors.

Results and Discussion

In this study, a range of different graphites was investigated for their suitability to serve as a low-capacity and high-stability component in graphite–Si electrodes. Their physical properties, provided by manufacturer, are presented in Table II, together with electrical-resistivity values, measured on graphite bars pressed at 2.5 t cm^{-2} , resulting in densities as indicated. The selection includes synthetic graphites with different particle-size distributions, where the d-values indicate the particle size at 10, 50 and 90 wt% of the cumulative particle mass; for example, the d₅₀-value is the median particle size of a sample. Accordingly, a d₁₀-value of 1.6 μm (KS6L) indicates that 10 wt% of the powder comprises particle sizes of 1.6 μm or smaller. The particle-size distributions of KS6L and SFG6L graphites are similar (Table II), whereas SFG6L exhibits a slightly higher anisometry of the particle shape.³³ Graphites of small particle size, as the ones presented here, are generally considered to be favorable complementary conductive additives with lower electric conductivity but higher volume density than carbon blacks. This is because they improve conduction paths and facilitate lower electrical resistivity of compressed electrodes.³³ This property can be beneficial for the electrode blends with an initially insulating Si fraction. The drawback of smaller particles is that they have higher specific surface areas (SSA) and, therefore, more electroactive surface needs to be passivated by SEI during the first cycle. As a result, the electrodes might suffer larger irreversible losses and, hence, lower Coulombic efficiency (C.E.).²⁹

The SSA of particles (based on the Brunauer–Emmett–Teller (BET) multilayer adsorption model) with larger grain size (in this study Actilion1 and SFG44) are about 10–15 $\text{m}^2 \text{g}^{-1}$ smaller than for KS6L and SFG6L. Actilion1 and SFG44 can be considered standard active materials for graphite electrodes. The fine fraction (d₁₀) of Actilion1 is somewhat smaller than the d₁₀-values of SFG44; i.e., 10% of the Actilion1 powder mass is comprised of particles that are smaller than 4.9 μm , whereas the value for SFG44 powder is 8.5 μm . The median particle size (d₅₀) of SFG44 is considerably larger than that of Actilion1, by about 10 μm . This can also be seen from the spread in particle sizes, i.e., the difference between d₁₀ and d₉₀. This parameter shows that 80 wt% of the particles in SFG44 powder exhibit particle sizes in the range from 8.5 μm to 48.4 μm ($\Delta = 39.9 \mu\text{m}$), whereas for the same fraction particle sizes in the Actilion1 powder are ranging from 4.9 μm to 28.8 μm ($\Delta = 23.9 \mu\text{m}$).

In general, graphites with higher crystallinity show lower electrical resistivity, which appears to be also the case for the resistivities reported in Table II. The electrical conductivity, the reciprocal of the electrical resistivity, was between 452 s cm^{-1} (KS6L) and 1098 s cm^{-1} (SFG44). This parameter might be relevant when the electrical conductivity of the electrode is of similar magnitude as the ionic conductivity of the electrolyte. For battery electrolytes, the latter lies in the range of 1–20 mS cm^{-1} at room temperature.³⁴ The ionic conductivity is therefore one to three orders of magnitude lower than the electrical conductivity and should have little impact on the internal resistance.³⁵ However, practical battery electrodes contain also conductive additive and binder, in addition to being porous. In contact with the electrolyte, the electrical conductivity can be lower.³⁶ On the other hand, Si particles are initially (before lithiation) poor electronic conductors and, therefore, might benefit from an electrically conducting network. In this respect, the SFG graphites show the highest conductivities, owing to their highest crystallinity among the graphites studied (Table II).

In our study, the graphites were used as matrices for Si with either 5 wt% or 20 wt% Si content. KS6L, SFG44 and Actilion1 were also tested as Si-free graphite electrodes, in order to

Table I. Electrode composition.

Sample	Graphite type	Graphite content /wt %	Silicon content ^{a)} /wt%	CB content ^{b)} /wt%	Binder content ^{c)} /wt%	Solid fraction (slurry)/%	Th. spec. charge/mAh g ⁻¹ Si/G	avg. mass loading/mg cm ⁻²	Areal capacity/μAh cm ⁻²	Electrode density/g ml ⁻¹	Electrode porosity/%
1	KS6L	95	0	1	4 (CMC: PAA)	32.8	372	6.67	2484.1	0.58	73
1-cal	KS6L	95	0	1	4 (CMC: PAA)	32.8	372	6.67	2484.1	1.24	43
2	KS6L	90	5	1	4 (CMC: PAA)	30.4	541	6.47	3498.3	0.63	71
3	KS6L	75	20	1	4 (CMC: PAA)	29.1	1046	6.16	6447.1	0.62	71
3-cal	KS6L	75	20	1	4 (CMC: PAA)	29.1	1046	6.16	6447.1	1.05	52
4	SFG6L	90	5	1	4 (CMC: PAA)	29.8	541	8.36	4521.0	0.60	72
5	SFG44	95	0	1	4 (CMC: PAA)	31.4	372	7.09	2638.8	0.58	73
6	SFG44	90	5	1	4 (CMC: PAA)	39.0	541	7.81	4223.0	0.69	69
7	SFG44	75	20	1	4 (CMC: PAA)	37.9	1046	8.09	8457.8	0.69	69
8	Actilion1	95	0	1	4 (CMC: PAA)	50.1	372	9.34	3474.1	0.84	62
9	Actilion1	90	5	1	4 (CMC: PAA)	48.0	541	7.46	4034.3	0.83	62
10	Actilion1	75	20	1	4 (CMC: PAA)	40.0	1046	7.13	7456.4	0.91	59
10-cal	Actilion1	75	20	1	4 (CMC: PAA)	40.0	1046	7.13	7456.4	1.08	51
11	SFG44: SFG6L	90 (8:1) ^{d)}	5	1	4 (CMC: PAA)	32.4	541	6.98	3778.3	0.64	71
12	SFG44: SFG6L	75 (8:1) ^{d)}	20	1	4 (CMC: PAA)	30.0	1046	5.64	5903.3	0.67	70

a) Si nanoparticles, 30–50 nm. b) Super C45. c) 1:1 mixture of CMC-Na and PAA. d) given in brackets is the SFG44-to-SFG6L ratio; for 90 wt% graphite contain 80 wt% SFG44 and 10 wt% SFG6L.

Table II. Properties of electro-active materials.

Graphite	d_{90} μm	d_{50} μm	d_{10} μm	$d_{90}-d_{10}$ μm	BET SSA $\text{m}^2 \text{g}^{-1}$	Crystallinity, XRDnm		Electrical resistivity $\Omega \cdot \text{cm}$ (@ density)
						Lc (002)	c/2 (002)	
Silicon					70–80			N.A. ^{a)}
KS6L	6.5	3.5	1.6	4.9	18.2	71	0.3359	2.21 (@ 1.86 g/cm^{-3})
SFG6L	6.7	3.7	1.8	4.9	16.6	91	0.3357	1.76 (@ 1.89 g/cm^{-3})
Actilion1	28.8	13.3	4.9	23.9	2.7	124	0.3360	N.A. ^{b)}
SFG44	48.4	24.0	8.5	39.9	4.5	440	0.3356	0.91 (@ 2.03 g/cm^{-3})

a) no information from manufacturer. b) no graphite bars could be prepared.

demonstrate that each graphite cycles with high reversibility and without any notable capacity loss in the chosen electrolyte formulation in the half-cells. The cycling-performance data, along with the C.E., are provided in Fig. S-1 is available online at stacks.iop.org/JES/167/100535/mmedia. For comparison, the cycling data of a graphite-free Si electrode (80 wt% Si) is shown in Fig. S-2. The cycling data of the Si-containing electrode formulations was correlated with electrode cross-section images of the pristine electrodes. As demonstrated in our previous work for the KS6L:Si mixtures, the amount of Si (and the electrode preparation) can have a profound effect on the morphology of the electrode coating and in particular on the distribution of the active materials.¹⁵

Electrodes comprising 90 wt% graphite and 5 wt% silicon.—The discharge capacities and corresponding C.E. are plotted in Figs. 1a & 1b. Essentially no difference was observed in terms of capacity retention and C.E. for graphite–Si electrodes containing either KS6L or SFG6L ($d_{90} < 7 \mu\text{m}$). Interestingly, the SFG44–Si electrode performs as well as the one with small particles, whereas the electrode containing Actilion1 is the only electrode formulation that shows accelerated capacity fading. All measured capacities of the KS6L, SFG6L and SFG44 graphite–Si formulations lie around the mean discharge capacity and within the corresponding standard deviation (2σ), which was determined from seven individual experiments with KS6L-Si (90:5) electrodes (Fig. S-3).

For long-term cycling, the C.E., shown in Fig. 2b, is comparatively high for Si containing electrodes (yet still too low for practical application in full cells), which is likely a result of the presence of

FEC in the electrolyte. As a result, differences between the KS6L, SFG6L and SFG44 formulations are insignificant, and even for the Actilion1-containing electrode only slightly lower values are observed. The differences between the electrode formulations with various graphites are clearly seen from the first-cycle C.E. in Fig. 2b, which ranges from 77.5% (Actilion1) to 88.8% (SFG44). A more meaningful comparison is the mean first-cycle C.E., averaged over four experiments for each formulation (Table III). The standard deviation for the Actilion1–Si electrode is larger than for the others. However, even though the mean C.E. of the Actilion1–Si electrode is slightly higher than the one of the cell displayed in Fig. 1b, this formulation still exhibits the lowest C.E. among the four compositions examined. In general, a higher C.E. would be expected from electrodes containing larger graphite particles,³⁷ SFG44 and Actilion1, due to the smaller SSA of the main active-material component (Table III). In a previous study by our group, a KS6–Si and a SLP30–Si blend (4.75 wt% Si) were also found to show similar capacity fading behaviors.³⁸ In accordance with the results reported herein, the C.E. of the SLP30–Si blend (SSA (SLP30) = $7.5 \text{ m}^2 \text{ g}^{-1}$) was higher than that for the KS6–Si blend that exhibited a larger SSA. As can be also seen in Table III, Si and graphite contribute nearly equally to the total SSA in these two cases, despite a large difference in their amounts. For the smaller graphite particles, KS6L and SFG6L, Si is responsible for merely $\approx 20\%$ of the total SSA. This correlation between SSA and C.E. applies to the SFG graphites and KS6L, but not to Actilion1. SFG44 displayed the highest reversibility on the first cycle, followed by SFG6L and KS6L, which exhibit similar C.E. values. Surprisingly,

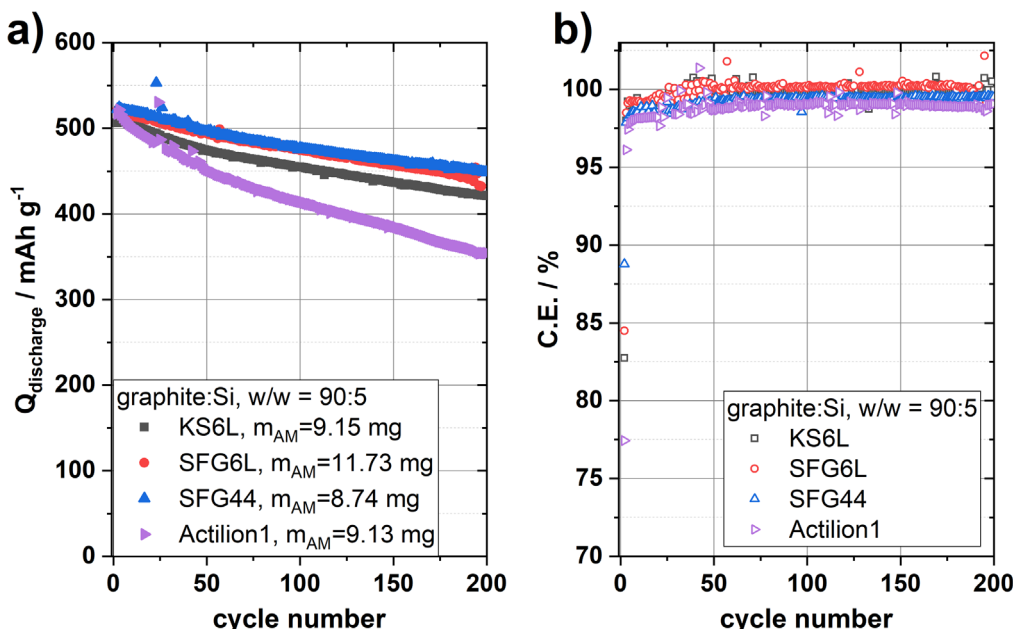


Figure 1. Discharge capacities (a) and corresponding Coulombic efficiencies (b) of graphite–silicon electrodes comprised of 90 wt% graphite (KS6L, SFG6L, SFG44, Actilion1) and 5 wt% Si (30–50 nm). In the legend of a) the active material loading of the electrode is provided.

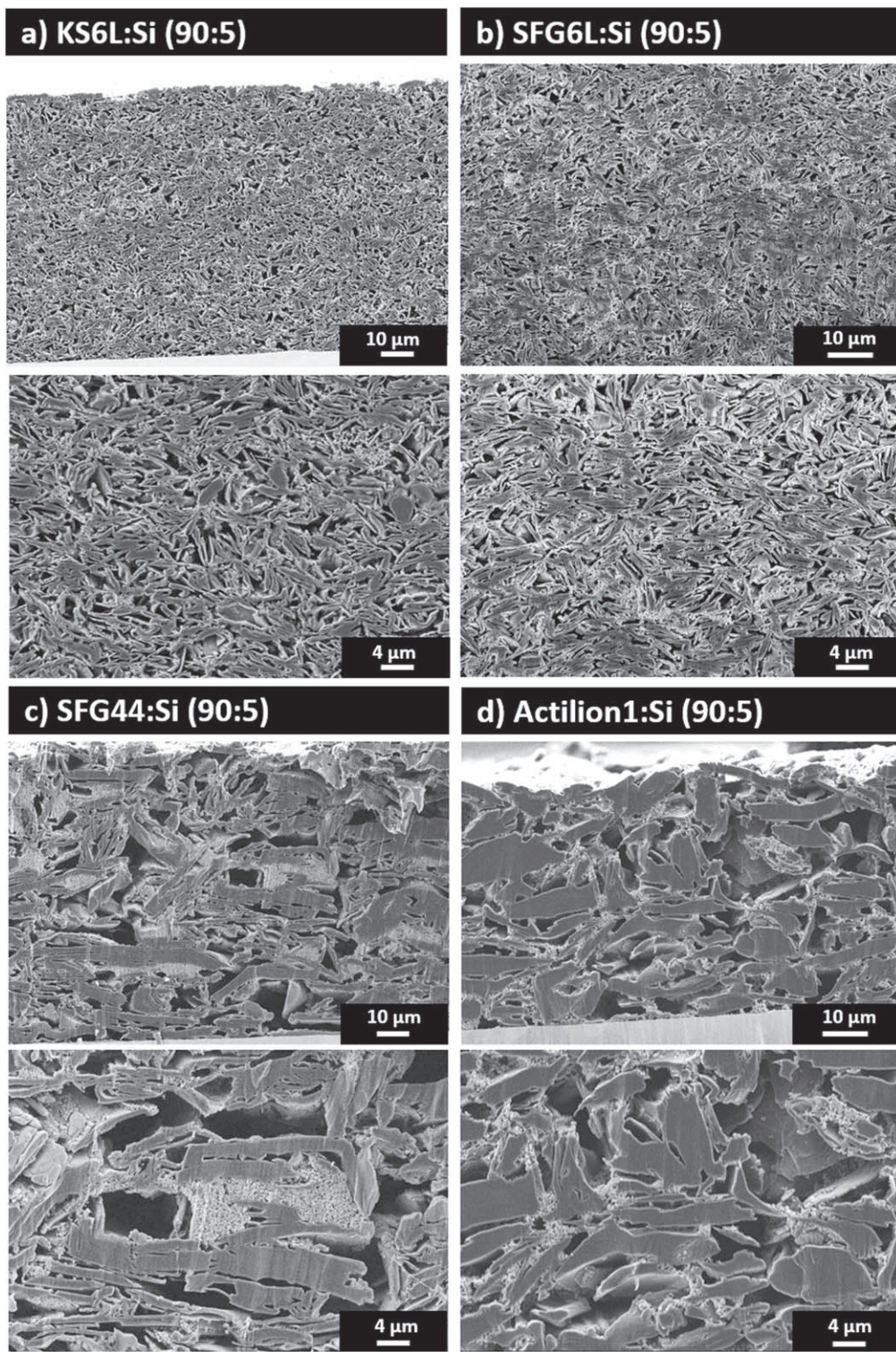


Figure 2. SEM cross-section images of graphite–Si (w/w = 90:5) electrodes containing KS6L (a), SFG6L (b), SFG44 (c) and Actilion1 (d) as graphite component.

Actilion1–Si has the lowest C.E., despite the graphite having the lowest SSA among all the graphites used in this study. The reason for this is unclear, but the observation is consistent with the rapid capacity fading. As will be discussed below, the poor performance could be related to the electrode morphology of the Actilion1–Si blend.

Regarding the use of FEC, it should be noted that the consumption of the electrolyte additive is strongly dependent on the active

material content (and consequently the electrode loading) of the expanding alloying or conversion material,^{8,15} and (absolute) FEC content,^{24,25} which correlates with electrolyte volume³⁹ used. The specific active material contents of the electrode formulations shown in Figs. 1 and 3 (5 wt% Si and 20 wt% Si) are provided in the legend (panel a). The results of Fig. 3 are discussed below. With respect to active material content there is one outlier in Fig. 1, the SFG6L formulation. The higher mass loading of this electrode leads to a

Table III. Electrode composition and properties.

Sample	Graphite type:Si	Graphite:Si	$\text{SSA}_{\text{graphite}} \text{ m}^2 \text{ g}^{-1}$ coating	$\text{SSA}_{\text{Si}}^{\text{a})} \text{ m}^2 \text{ g}^{-1}$ coating	Total SSA $\text{m}^2 \text{ g}^{-1}$ coating	C.E., 1st cycle ^{b)}
2	KS6L:Si	90:5	16.38	3.75	20.13	0.826 (± 0.015)
4	SFG6L:Si	90:5	14.94	3.75	18.69	0.828 (± 0.017)
6	SFG44:Si	90:5	4.05	3.75	7.80	0.899 (± 0.017)
9	Actilion1:Si	90:5	2.43	3.75	6.18	0.815 (± 0.063)

a) assuming a SSA of $75 \text{ m}^2 \text{ g}^{-1}$. b) mean C.E. and standard deviation (1σ) determined in four experiments.

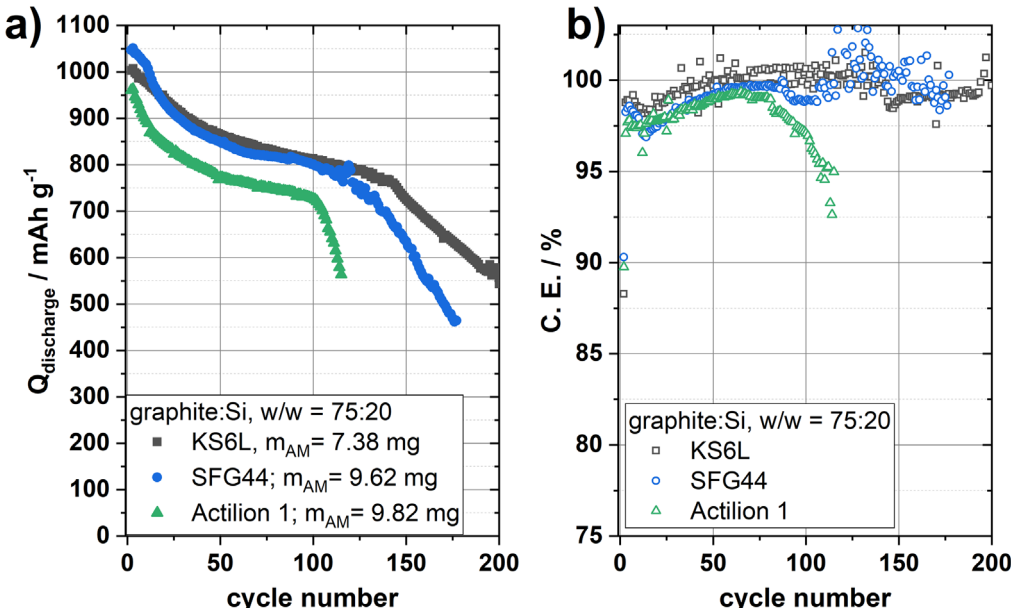


Figure 3. Discharge capacities (a) and corresponding Coulombic efficiencies (b) of graphite–silicon electrodes comprised of 75 wt% graphite (KS6L, SFG6L, SFG44, Actilion1) and 20 wt% Si (30–50 nm). In the legend of a) the active material loading of the electrode is provided.

visible onset of more rapid capacity fade at the end of the first 200 cycles, which is attributed to the complete consumption of FEC in the electrolyte. Electrodes with lower loadings maintain their relatively linear capacity fade beyond the 200th cycle. We have reported¹⁵ dependence of the maximum cycle life of the Si content of graphite–Si blends in more detail previously.

The differential capacity (dQ/dE) vs potential (E vs Li^+/Li) and cycle number was plotted as heat maps¹⁹ (example between regular dQ/dE plot given in Fig. S-4a) for formulations with either of the four graphites, 0 wt% Si (Fig. S-4b) and 5 wt% Si (Fig. S-4c), respectively. The reaction potentials of Si-free graphite electrodes (Fig. S-4a) and corresponding formulations with 5 wt% Si (Fig. S-4c) are located as distinct lines at similar potentials (the dQ/dE maps are dominated by the graphite features, due to the high fraction of graphite and its distinct reaction plateaus, as compared to the sloping potential profiles of the amorphous Si phases). It can be noted that the dQ/dE peaks in graphite–Si blends shift, with increasing cycle number, towards lower potentials upon lithiation and towards higher potentials upon delithiation. This finding is in accordance with an increasing voltage hysteresis reported in our previous work.¹⁵ The delithiation plateau of the crystalline Si phase at around 500 mV vs Li^+/Li ¹² disappears within the course of the first 40–50 cycles. Thereafter, it is only the amorphous Si phase that is cycled.

The morphology of electrodes with large differences in particle size is shown in the cross-section micrographs in Figs. 2a–2d. Electrodes containing KS6L- and SFG6L exhibited similar electrode morphologies, where the basal plane of the anisotropic graphite particles is aligned mainly horizontally relative to the current collector. Because of the comparatively small particle size, the particle packing is rather tight and no larger void spaces are present. In general, the Si particles are well distributed within the graphite

matrix, sandwiched between the graphite particles. In few locations the agglomerated Si forms domains of a few μm in size. By contrast, large graphite particles create larger void spaces in the uncalendered electrodes. In other words, the particles are packed less efficiently. In these electrodes, the material distribution is inhomogeneous: the Si fraction forms large agglomerations up to $10 \mu\text{m}$ in size. They are thought to be detrimental to the electrode performance, because these domains can induce local hot spots for stress within the electrode matrix that may affect adjacent regions as well, which in turn would promote electrode disintegration and loss of electrical contact. According to simulations by Müller et al.,⁴⁰ inhomogeneities also affect the mass transport properties and can lead to additional overpotentials during the cell reactions. In fact, the dilatometry experiments by Gómez-Cámer et al.³⁸ on KS6-Si and SLP30-Si blends show a larger relative height change for electrodes comprising the larger-sized SLP30 graphite.

A comparison between the electrode morphologies of the two large-size graphites is shown in the micrographs displayed in Figs. 2c and 2d. The platelet-shaped SFG44 exhibits a high basal and a small prismatic surface, the length and width of the basal surface of up to $30 \mu\text{m}$ have been measured. Even if the majority of the particles still align parallel to the current collector (basal plane parallel to the current collector), there is typically less continuity than in electrodes prepared with graphite types of smaller particle size. In the Actilion1-Si electrodes, the particles appear to be oriented more randomly, exhibiting a wider particle cross-section, which is likely due to particles that are turned out of the horizontal plane (the basal plane is facing the observer). This leads to a clear change in the electrode structure. Interestingly, smaller Si agglomerates are observed than in the corresponding SFG44–Si blend. Both particle orientation and particle size have an important role in

maintaining pathways for electron conduction.⁴¹ The broader particle-size distribution of SFG44 might be more favorable in this case, as it covers a broader range of length scales for electronic contacts. Another factor that is difficult to deduce from the electrode cross-sections alone is the electronic connection to Si domains. This depends, on the one hand, on the contact with the surrounding graphite matrix and the penetration of these domains with carbon black and, on the other hand, on the fine fraction of the graphite powder. How well the materials blend might depend critically on the way the electrode slurry is prepared and on the solidification behavior of the electrode coatings.

The formation of the final electrode morphology during the drying of the cast electrode slurry is a dynamic and complex process.⁴² The pore structure of the electrode, for instance, can be dependent strongly on the evaporation rate of the slurry solvent, which in itself is a function of temperature and humidity.⁴³ Particles settle during drying and might agglomerate in the process. At the same time binder migration can occur, changing the adhesion and cohesion properties of the electrode coating.^{43,44} The sedimentation rate was controlled by adjustments of the solvent concentration (or the solid content of the slurry) depending on the graphite type.⁴⁵ This lead to comparatively high solid fractions in Actilion1-containing slurries with 0 wt% or 5 wt% Si (Table I). Such high solid fractions are typically more relevant for upscaling of electrode slurries, where different mixing equipment changes the rheological properties of the electrode slurry. On a laboratory scale, however, solid fractions can be quite different, depending on the mixing method chosen; typically they lie in the range of 20–40 wt%.^{14,31} As the solid fraction of the slurry changes, so does its rheology. As a result, different electrode morphologies develop during film solidification. This process is difficult to control in a laboratory setting. These parameters have a subtle, yet vital, role in the performance of an electrode coating that translate into different morphologies and fading rates, as observed in the case of the Actilion1–Si formulation (Fig. 2a).

On top of the electrode preparation conditions, the choice, amounts and properties of the slurry components (μm -sized graphite particles, nano-sized Si and CB particles) have an influence on the formation of the electrode morphology:

- (1) As mentioned above, SFG44 has a broader particle-size distribution than Actilion1, which could be beneficial for the interconnectivity of the active material, as a broader range of length scales is covered by the particles. However, if the particle size would be a parameter that comes into play, then based on the results obtained with the small-size graphites (KS6L and SFG6L), Actilion1 would be expected to perform better than SFG44, as the graphite powder contains a larger fraction of small particles. Therefore, the particle alignment and the void space, created as the electrode coating dries, might be just as important.
- (2) Resilient, water-soluble binders are current state-of-the-art for Si electrodes and have also been used in this work, specifically a mixture of CMC-Na and PAA. Water-soluble binders tend to form more resilient binder–particle networks through entanglement and cross-linking,^{46,47} which was demonstrated recently in experiments by Gómez-Cámer et al.³⁸ and Tranchot et al.⁴⁸ Their low swellability in the electrolyte is another reason for the higher resilience.^{49–51} Especially, when used in larger amounts (>4–5 wt%), they can also fulfill an important function of protecting electrode surface from degradation processes.^{19,50,52} The SEI layer composition is also subjected to changes depending on the binder content.⁵³ Binder interactions with other electrode components, the active material(s) and carbon black, has a decisive impact on the overall particle distribution and the percolating conductive network.^{54–56} As surfactants, binders tend to adsorb strongly onto nanosized materials, which ultimately leads to changes in the mechanical properties of the composite as a result of missing particle interconnections.

- (3) Carbon black (CB) acts as conductive additive to ensure electronic conductivity within the particle network. Its amount was fixed in this study to 1 wt%. The aggregation of CB is determined by the binder–CB interactions and further by the choice and amount of solvent.^{54,57} Both CB and Si exhibit similarly high SSA, meaning that on some level during the slurry preparation, they will compete over the available binder.¹⁹ For given Si, CB and binder amounts, the Si–CB–binder SSA-ratio and, thus, the binder coverage on those particles remains the same for all composites in the series. As a result of the higher surface energy of the nanoparticles, it is expected that the binder interacts predominantly with these. The strength of the interaction further depends on the surface properties (e.g. the zeta-potential⁵⁸) of the particles (i.e. Si particles: native SiO_2 layer; CB: hydrophobic, with polar surface groups). This can be seen for instance in the formation of more resilient Si–binder networks during the slurry preparation and drying process in the presence of organic acids at low pH.^{20,59,60} Because the major SSA fraction in blends with 5 wt% Si still falls on graphite (Table III), some degree of binder redistribution is expected (but most likely to be minor).

Electrodes comprising 75 wt% graphite and 20 wt% silicon.—

The differences between various types of graphite become more apparent when the Si content is increased. In Fig. 3, the discharge capacities and the C.E. are shown for electrodes containing 20 wt% Si and 75 wt% graphite (KS6L, SFG44 or Actilion1). The KS6L sample stands representative for samples containing graphite with small particle sizes, as based on the results of the previous section, similar electrode morphologies and electrochemical behavior were to be expected from corresponding SFG6L–Si electrodes.

Actilion1 suffers from rapid fading from the very beginning, while both SFG44 and KS6L show higher initial discharge capacities than Actilion1. However, when the capacity retention of each formulation is calculated with respect to the first-cycle discharge capacity, all samples end up at relatively similar values after 100 cycles, with capacity retentions of 80.7% (KS6L), 76.2% (SFG44) and 75.5% (Actilion1). The faster initial fading of the Actilion1–Si blend in this series could be partly ascribed to the higher electrode density of this formulation, which is, with an average density of 0.91 g ml^{-1} , higher by 0.22 g ml^{-1} than the corresponding SFG44–Si blend and by 0.29 g ml^{-1} higher than the KS6L–Si blend (Table I). If the electrode density is expressed in terms of electrode porosity, it can be noted that between an electrode density of 0.65 g ml^{-1} (ca. 70% porosity) and 0.9 g ml^{-1} (ca. 60% porosity), there is a porosity difference of only 10%. However, even such small differences have been reported to adversely affect cycle life of Si electrodes.^{19,61}

Differences in cycle life, i.e. the point at which accelerated capacity fading occurs, are likely to be a result of variations in mass loadings between different formulations and the effective electrode SSA. Even small differences in mass loading can have a profound effect on the onset of capacity fading in these electrodes, as the FEC electrolyte additive is used up at different times.^{8,15,24,25,39} More important than the actual mass loading is the effective electrode SSA, that is, the electroactive surface area (EASA). It determines how much electrode surface needs to be covered by the SEI layer and, therefore, how much of the additive it will consume for its formation. For the current discussion, the precise onset of rapid electrode breakdown is not crucial, as the results unambiguously show that a strong capacity fade is to be expected as the Si content is raised. A drop in capacity from 1000 mAh g^{-1} to 800 mAh g^{-1} corresponds to the often-reported capacity-loss threshold for batteries of 80%. For the graphite–Si formulations used in this study, with 20 wt% Si content, this threshold would be reached already after 100–125 cycles (for SFG44- and KS6L-containing electrodes) and even earlier, after less than 50 cycles, for the Actilion1

formulation. Any full-cell would break down after only very few cycles, making it of little practical use.

The first-cycle C.E.s lie in a narrow range from 88.2% (KS6L) to 90.3% (SFG44). The mean C.E. values and corresponding standard deviations are given in Table IV. Surprisingly, the first-cycle C.E. values are in general higher with 20 wt% than with 5 wt% of Si, while one would expect an opposite trend with increasing Si contents (and thus the electrode SSA). Table IV shows that the graphite contributes only 10%–20% to the total SSA in blended electrodes with large graphite particles (an increase in SSA of \approx 10–11 m^2g^{-1} compared to the samples presented in Table III), whereas in the KS6L–Si electrode still about half of the SSA originates from the graphite (an SSA increase of $8.52 \text{ m}^2\text{g}^{-1}$). One issue with the correlation of the SSA with the C.E. is the fact that the SSA given in Tables III and IV are estimations based on the SSA of the individual electrode components. In a previous publication, our group determined that the EASA is in fact 2–3 times smaller than the SSA.⁶² Therefore, the SSA merely marks the maximum surface area. Following the general argument that the C.E. depends on the EASA,²⁸ it would appear that despite larger amount of nanoparticles, the EASA has decreased.

In a similar experimental series, it was observed by Wetjen et al.³¹ that the C.E. did not change significantly with increasing Si content. In their samples the SSA increased with Si content from 12 m^2g^{-1} (20 wt% Si) to 26 m^2g^{-1} (60 wt% Si). That is, with respect to the SSA of the formulations, the C.E. per area seems to decrease with increasing SSA. To explain this counterintuitive behavior, the authors suggested to compare the formulations in terms of SSA per capacity unit ($\text{m}^2 \text{Ah}^{-1}$), which was constant for all electrodes. However, this ratio does not seem to be constant in our setup for electrodes with the same active materials but different Si contents. Instead, we suspect that the SSA is smaller than anticipated because of Si agglomeration. These agglomerates can be viewed as secondary particles, where the number of particle–particle contacts is higher and the surface exposed to the electrolyte is effectively reduced.

The dQ/dE maps (Fig. S-4d) show a stronger polarization during lithiation and delithiation, when 20 wt% Si is used in the graphite–Si blends. The dQ/dE lithiation peaks have shifted below 100 mV and the slopes are steeper than in formulations with only 5 wt% Si. In the region between 150–250 mV vs Li⁺/Li, the alloying reaction of Si is now visible due to the higher Si fraction. During the delithiation, the conversion of the crystalline Si phase dominates the dQ/dE maps. As this peak fades, an almost linear sloping profile of the delithiation process remains,¹⁵ exhibiting no distinct dQ/dE peaks. In addition, the higher delithiation rate reduces the intensity of dQ/dE peaks even more.

Compared to the cross-section of the KS6L–Si, the electrodes, containing large graphite particles with 20% of Si, show a considerably different structure (Fig. 4). In the KS6L formulation, a lot of the additional Si has accumulated in larger domains, while only small fractions of Si are embedded in the surrounding graphite matrix (Fig. 4a). When the particle size is increased and the overall content of graphite decreased, such as in electrodes containing either SFG44 or Actilion1, an “inverse morphology” is generated, where the much larger graphite particles are embedded into a matrix of Si. It is worth noting that Wetjen et al.³¹ and Dose et al.⁶³ observed similar electrode morphologies using large graphite particles (T311 (ca. 20 μm , according to authors), SGL Carbon and MAGE (d₅₀ =

23.5 μm), Hitatchi Chemicals, respectively) with Si contents in the range of 15–20 wt%. This shows a strong dependence between the graphite-particle size and electrode morphology. In these electrodes, the distance between graphite particles is increased because more and more volume is occupied by Si. The results are in accordance with observations from the above-mentioned cross-section analysis.³¹ The electrode morphology of electrodes containing large graphite particles and high Si amounts could eventually compromise the electrical conductivity of the electrode.

Comparing the cross-section images of electrodes with 20% of Si to the ones of SFG44 and Actilion1 with only 5 wt% Si, it is observed that the general particle alignment of the SFG44- and Actilion1-particles has not changed when the Si content is increased: in the SFG44–Si electrode the graphite particles are mainly horizontally aligned, whereas the Actilion1–Si electrode has a larger fraction of particles that are out of the electrode plane. This has an impact on electrode properties, such as the tortuosity.

Moreover, the visible empty voids in the cross-section of the SFG44–Si blends are greatly reduced with a Si content of 20 wt%. In the Actilion1–Si blend, a larger void space is observed, as compared to the SFG44–Si blend. This is somewhat counterintuitive, considering that the electrode density of the as-received (after drying) formulations is higher for the former composition. However, Si domains consist of nanoparticles, which themselves can generate a considerable fraction of void space within the domains,⁶³ which could ultimately lead to an overall smaller electrode density as is the case for the SFG44–Si blend. Unfortunately, this discussion leaves room for speculation, as the cross-sections represent only a single slice of the electrode coating. Tomographic data would be helpful to gain a better understanding of the particle distribution and connectivity in these three-dimensional particle networks. Because of the vastly different length scales of Si particles (tens of nm) and graphite particles (tens of μm), it is challenging to probe with currently available techniques a representative volume of the coating with the required resolution for both materials.

Calendered electrodes.—Following the conclusion of the previous section that the SFG44–Si blend exhibits a denser electrode morphology than the corresponding Actilion1–Si blend. In an attempt to improve the performance of the latter, the electrode was densified. The calendering process brings particles into closer contact with each other, which improves the electron conduction pathways during the electrochemical reaction. Furthermore, in a pristine electrode, empty void spaces are reduced when the particles are pressed closer together. However, densification could be in turn associated with a penalty for the ionic conduction, as the electrolyte volume within the electrode decreases with the decreasing pore volume. For the experiment, we have picked the KS6L–Si blend as the reference electrode. Maximum electrode densities of up to 1.1 g cm^{-3} were achieved for formulations with 20 wt% Si. Increasing the roll pressure or decreasing the gap further did not yield denser coatings, which indicates the limit of the in-house calender. For comparison, the electrode densities are reported in Table I. Typical density after casting and drying is 0.6 g ml^{-1} for KS6L-containing electrodes. Actilion1-blends exhibit higher densities to start with (Table I). Compared to the density of commercial electrodes (up to 1.5 – 1.6 g ml^{-1}),¹ the electrode densities achieved herein can be considered medium dense at best. The maximum achievable electrode density decreased with increasing Si content.

Table IV. Electrode compositions.

Sample	Graphite type	Graphite:Si	SSA _{graphite} $\text{m}^{-2} \text{ g}^{-1}$ _{coating}	SSA _{Si} ^{a)} $\text{m}^{-2} \text{ g}^{-1}$ _{coating}	Total SSA $\text{m}^{-2} \text{ g}^{-1}$ _{coating}	C.E., 1st cycle ^{b)}
3	KS6L:Si	75:20	13.65	15	28.65	0.881 (± 0.006)
7	SFG44:Si	75:20	3.38	15	18.38	0.896 (± 0.010)
10	Actilion1:Si	75:20	2.03	15	17.03	0.904 (± 0.012)

a) assuming a SSA of $75 \text{ m}^2\text{g}^{-1}$. b) mean C.E. and standard deviation (1σ) determined in four experiments.

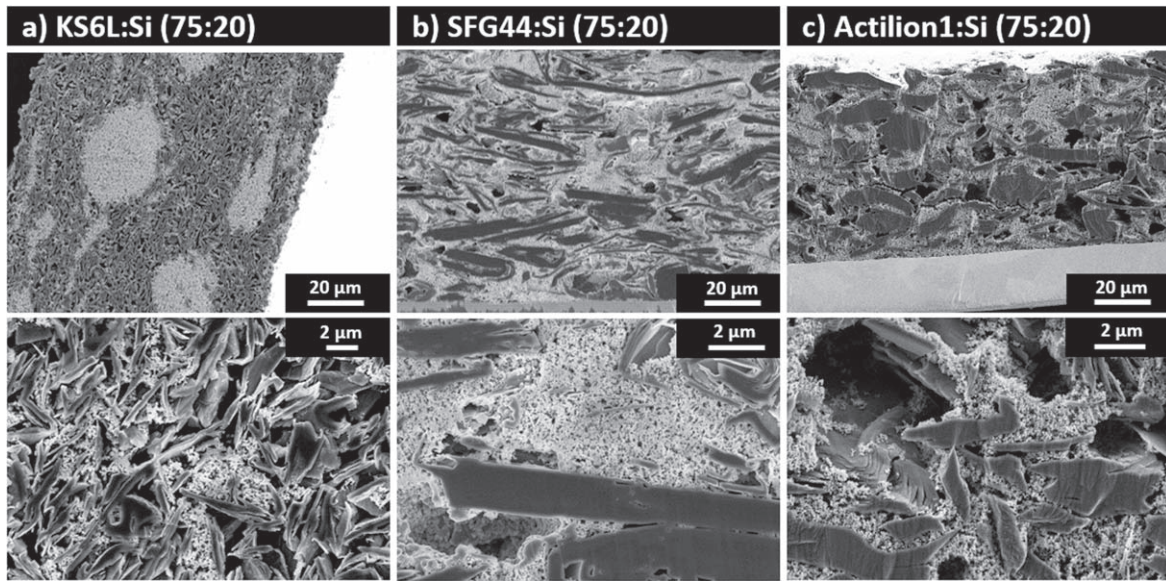


Figure 4. SEM cross-section images of graphite–Si electrodes (w/w = 75:20), containing KS6L (a), SFG44 (b) and Actilion1 (c).

Both graphite and nanoparticles display spring-back behavior, which can cause a relaxation of the compressed electrodes. The comparison of the cycling results between calendered and uncalendered samples in Fig. 5 demonstrates that even a small increase in the electrode density can have an adverse effect on capacity retention.

The initial discharge capacities of the calendered electrodes are lower than those obtained for the corresponding uncalendered samples. The Actilion1–Si blend loses more capacity on the initial cycles than the KS6L–Si blend, meaning that with the smaller KS6L particles more capacity can be retained on the first cycles. This result can be explained mechanically in the context of different electrode morphologies, graphite particle size and inhomogeneous particle distributions.

Both electrodes exhibit relatively large areas of agglomerated Si particles. Small graphite particles, such as KS6L surround these areas without forming larger voids in the coating. Figuratively speaking, it is less difficult to surround agglomerated areas with a large number of small particles than with a small number of larger particles. This will also impact the capability of compensating volume changes in these domains, since small particles will be able to respond more flexibly to the stress by reorientation to expanding areas. Horizontally aligned particles could further rearrange volume changes by sliding against each other (after all, graphite is a commonly used component in lubricants; Scheme 1). This can be an advantage when the distribution of the active materials is inhomogeneous and one component exhibits a much larger expansion coefficient than the other, since build-up of internal stress can be reduced. This is partly reflected in the rapid capacity fade of Actilion1 blends. In case of a calendered electrode, there is additionally less void space available that could buffer the expansion of Si domains. For (graphite-free) Si electrodes, there is a strong correlation between electrode porosity and cycle life.⁶¹ In addition, “breathing effects,” specifically Si particle movements and redistributions under repeated volume changes,²¹ in a denser electrode environment could lead to faster disintegration of electrode. Therefore, such coatings may endure higher internal stresses leading to faster detrimental morphological changes and associated rapid capacity fade. This is generally in accordance with earlier findings by Gómez-Cámer et al.,³⁸ showing larger volume changes of graphite–Si blends that contained a graphite type with larger particle sizes. One can only speculate that this problem is amplified by increasing the Si content. Simulations suggest that locally induced stress, for instance due to heterogeneous volume changes within the electrode, may adversely affect transport properties of adjacent

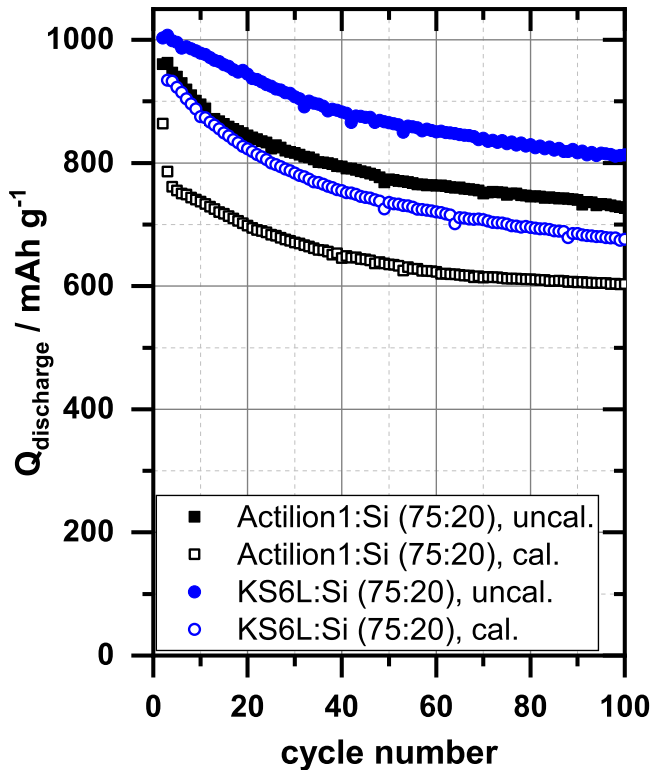
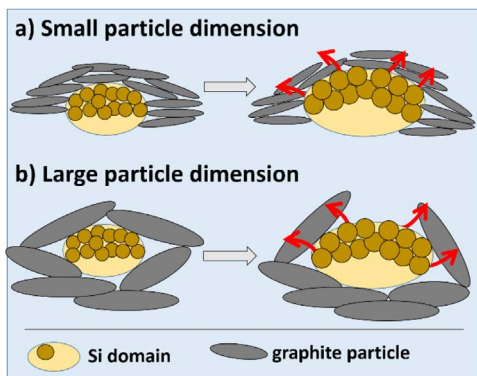


Figure 5. Comparison between the capacity fade of calendered (open symbols) and uncalendered (full symbols) electrodes for graphite–Si blends consisting of KS6L:Si (blue) and Actilion1:Si (black) with Si contents of 20 wt%.

domains as well, and thus making the problem even more severe.⁴⁰ In the above comparison between Actilion1 and KS6L blends, this appears to be one of the main reasons for the fast initial capacity fade of the Actilion1–Si blend. Because of the rapid initial degradation, the rate of capacity fading slows down, while in the KS6L–Si blend the degradation occurs in smaller steps over more cycles, leading to an overall steeper fading slope of the capacity profile. In more general terms it can be stated that calendering has an adverse effect on the capacity retention of graphite–Si blends.



Scheme 1. Sketch of different responses of a graphite matrix towards a volume expansion of the enclosed Si domain in a graphite/Si blend (small graphite particles, a, vs large graphite articles, b).

As a side remark, it was observed that the calendered electrodes had a delayed onset of electrode failure (the point at which the capacity starts to decrease rapidly), which we attributed to the decrease of electroactive surface area after densification and the correspondingly reduced rate of electrolyte additive consumption.

Blends of small and large graphite particles.—As mentioned previously, KS6L and smaller graphites are commonly used as conductive additives in cathodes compositions,³³ rather than as the main active material. In the present study, these particles performed best in combination with small fractions of Si. Larger graphite particles, which are typically used for negative electrodes, performed rather poorly in graphite–Si electrodes when the Si content reached 20 wt%. In case of Actilion1, a faster capacity fade was observed even for low Si content of 5 wt% (Fig. 1). In addition, we tested blends comprising of the two SFG graphites with 5 and 20 wt% Si, respectively. SFG44 and SFG6L were mixed in a ratio of 8:1 by weight (from here onwards referred to as “SFG blends”). The motivation to test this blend was to reach a smaller electrode SSA than in the KS6L–Si blend while maintaining the high capacity retention and improving the particle distribution of the graphite–Si blends by increasing the fine-fraction of the graphite powder. The performance of these SFG blends was compared to the corresponding single-graphite formulations. The cycling data is shown in Figs. 6a and 6b.

For the SFG blend containing 5 wt% Si, the discharge capacity and capacity retention are slightly improved with respect to the corresponding KS6L–Si electrode. In terms of discharge capacity, the SFG blend follows the behavior of the individual SFG-containing electrode formulations (Fig. 1). In the direct comparison of SFG44:Si (90:5) and the SFG blend (Fig. 6a), the discharge capacities coincide and the capacity retention is similar as well. The first-cycle C.E. shown in Fig. 6b has increased by about 7% (KS6L:Si, w/w = 90:5) to 90.6% (± 0.012) (mean C.E. over four experiments), which is only slightly lower than the C.E. of the SFG44:Si (90:5) formulation (Table III).

When the Si content is increased to 20 wt%, the initial discharge capacities of the SFG blend and the KS6L electrode are similar. However, after only a few cycles, the discharge capacity of the electrode with SFG blend drops significantly. After around 50 cycles, the capacity fading slows down. In contrast, the KS6L–Si electrode retains initially more of its capacity, but over the course of \approx 125 cycles, both electrode formulations approach similar capacity values. At this point, rapid cell failure sets in for the KS6L–Si electrode, presumably due to a lack of FEC in the electrolyte. The SFG blend behaves differently at the onset of cell failure and shows scattered capacity values, which has been ascribed previously to short-circuits due to dendrite growth.⁶⁴ Interestingly, when the performance of the SFG blend is compared to the SFG44:Si (75:20) formulation, the electrode shows identical features regarding

the capacity fade. The difference between the two formulations is merely the initial discharge capacity of approx 50 mAh g^{-1} for the SFG44:SFG6L:Si (67:8:20) formulation. As shown in Fig. S-4, curves coincide, when the data of the SFG blend is shifted by this initial capacity difference (the same applies to the C.E., Fig. 6d).

The first-cycle C.E. of 88.3% for the SFG blend is smaller than the value for the SFG44 electrode, but similar to the KS6L electrode (the two points lie on top of each other in Fig. 6d). With exception of the initial C.E., the SFG blend follows the behavior of the corresponding SFG44 formulation, as in the previous case with 5 wt% Si. The fact that a significant drop in capacity can be noted in both cases after about 15 cycles demonstrates that this drop is associated with the presence of larger graphite particles. This capacity loss coincides with a distinct minimum in the C.E. of the formulations comprising both SFG44 and the SFG blend (Fig. 6d). This feature is less pronounced in the KS6L-containing formulation. This C.E. minimum means that in these cycles considerably more active material has been lithiated than delithiated. A likely origin is particle disconnection and an accompanying loss in cyclable active material. The disconnection is presumably related to particle rearrangements, which have been reported for pure Si anodes as a result of the expansion/contraction behavior of Si.²¹ A rather sudden drop in the discharge capacity could indicate that in course of the rearrangement some of the active material is rendered inactive.

As for the previous electrode formulations, cross-sections have been prepared from the new electrodes (Fig. 7). In comparison to the cross-section images of the SFG44–Si electrode (90:5) in Fig. 2, one can see that a good part of the previously observed empty space generated by the large graphite particles has disappeared, owing to the presence of the smaller SFG6L particles. The electrode still exhibits agglomerated Si domains of several microns in length and width, but they do not seem to affect the capacity retention. This result is in accordance with the results shown in Fig. 1, where the SFG44–Si electrode performs as well as the formulations with the smaller graphites KS6L or SFG6L. In the case of electrodes with 20 wt% Si, the typical domain formation of Si can be observed, as shown earlier for the other graphite–Si formulations (Fig. 4). It can be noted that, compared to the SFG44:Si (75:20) formulation, the graphite particles in the SFG blend appear less aligned horizontally (Fig. 7), which could be one reason why the electrode performance is inferior to that of the original two-component formulation (Fig. 4b) in the cycling test. A positive aspect from the addition of a fraction of small particles is seen in Fig. 7f, where smaller graphite particles are embedded in the Si matrix. On the other hand, the supposedly improved particle distribution is reflected neither in an improved initial discharge capacity (as in the case of 5 wt% Si) nor in better capacity retention.

Conclusions

In electrode blends comprising graphite and Si, graphite takes on the role as both active material and conductive additive. The material requirements for an active material (e.g. small surface area) and a conductive additive (e.g. low electronic resistivity) can be quite different in nature. We have looked into several graphite properties, such as particle-size, particle-size distribution, conductivity, crystallinity and surface area. In contrast to a previous study,²³ our results demonstrate that larger graphite particles are not necessarily leading to worse performance (case of SFG44) than formulations with smaller particles (KS6L), despite a more inhomogeneous distribution of the electrode components. Here, a broader particle-size-distribution helps to achieve equally good capacity retention with an overall larger graphite particle-size due to the ability of the fine fraction of the graphite to penetrate into the agglomerated Si domains, filling part of the void space created by the larger particles.

In the presence of only 5 wt% Si, large Si domains are found between the large graphite particles, which are potential spots of increased stress and strain during the expansion of Si upon lithiation. A more homogeneous material intermixing was achieved only when

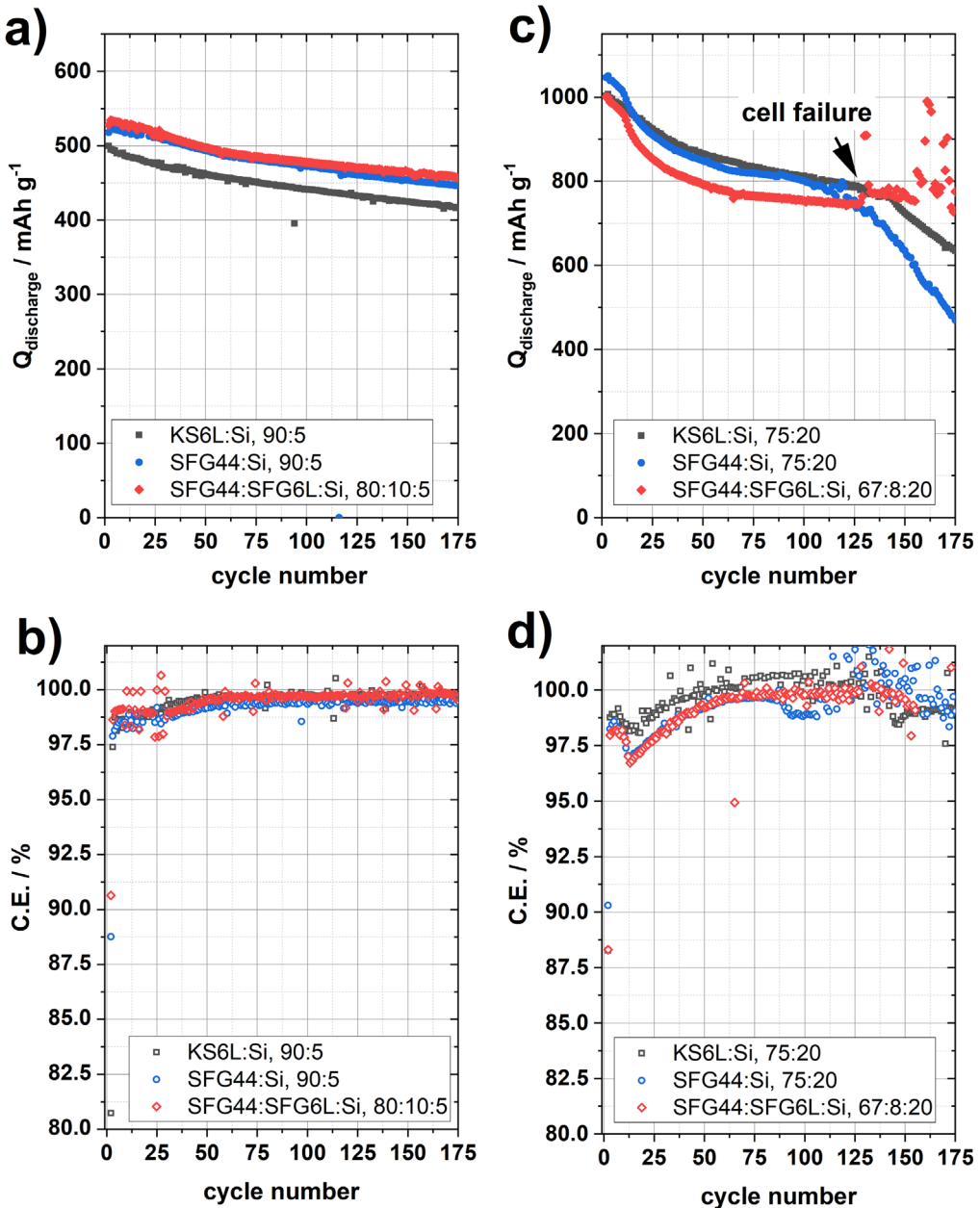


Figure 6. Comparison of the electrochemical performance between graphite–Si electrodes with KS6L and SFG44 as the sole graphite component and a graphite blend containing both SFG44 and SFG6L (w/w = 8:1). (a) and (c) galvanostatic cycling and (b) and (d) C.E. The Si content was either 5 (a), (b) or 20 (c), (d) wt %.

graphites with smaller particle sizes were added to the electrodes. When the Si content is raised to 20 wt% and the graphite dimensions are in the range of tens of μm , the electrodes show an “inverse morphology,” where the Si-fraction forms the electrode matrix with embedded graphite particles (graphite in silicon). This is in stark contrast to electrodes containing smaller graphite particles, such as KS6L, where the main matrix is still provided by the graphite fraction (silicon in graphite), but which does not prevent Si agglomeration. The comparison between two different graphites with larger particle sizes, SFG44 ($d_{90} < 48.4 \mu\text{m}$) and Actilion1 ($d_{90} < 28.8 \mu\text{m}$), shows that a broad particle-size distribution alone is not the only parameter that is decisive for the performance of the electrode. SFG44 showed a clear horizontal alignment for the largest fraction of the graphite. The morphology of Actilion1-Si electrodes had a tendency to form larger void spaces with a more random particle orientation. The morphological differences are also a result of the rheological properties of the electrode slurry and the drying

conditions of the coatings, which can be partly linked back to the graphite properties as well.

Densification of electrodes in order to mitigate adverse porosity effects resulted in significantly lower initial discharge capacities and poorer capacity retention. An improvement in Coulombic efficiency was achieved by blending a fraction of small graphite particles with a large type. The graphite blends did not change the capacity retention, when compared to electrodes with a single graphite type. On the long term, the consumption of FEC is reduced resulting in higher Coulombic efficiency, which is expected to prolong the cycle life.

Acknowledgments

The authors acknowledge financial support by Innosuisse (project number 18254.2).

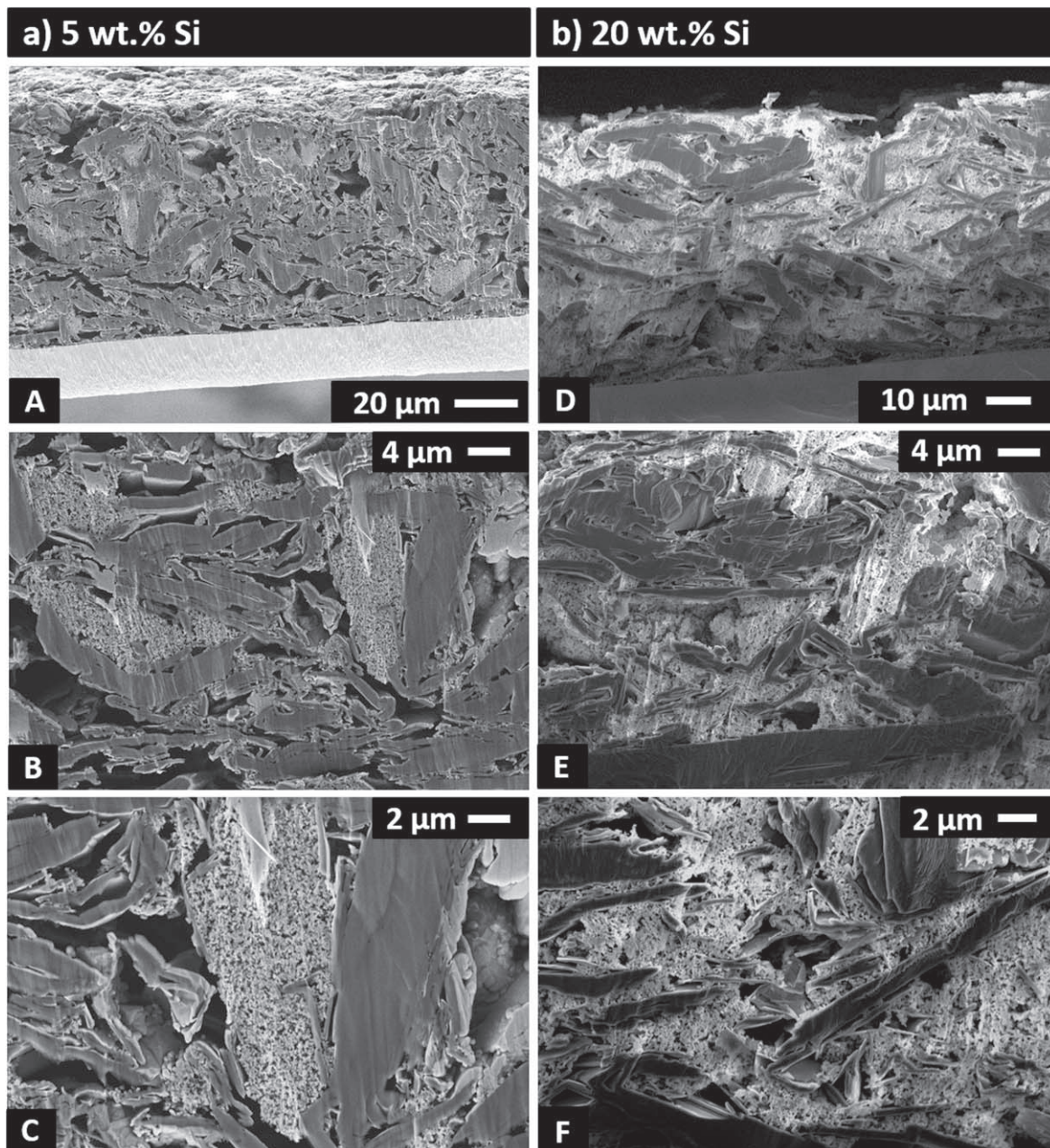


Figure 7. Cross-section micrographs of graphite–Si electrodes containing a blend of SFG44 and SFG6L (w/w = 8:1) and Si nanoparticles with 5 wt% Si (a)–(c) and 20 wt% Si (d)–(f), respectively.

ORCID

Yuri Surace <https://orcid.org/0000-0003-4376-6914>
 Petr Novák <https://orcid.org/0000-0001-6993-5021>
 Sigit Trabesinger <https://orcid.org/0000-0001-5878-300X>

References

- E. J. Berg, C. Villevieille, D. Streich, S. Trabesinger, and P. Novák, “Rechargeable batteries: grasping for the limits of chemistry.” *J. Electrochem. Soc.*, **162**, A2468 (2015).
- M. Holzapfel, H. Buqa, F. Krumeich, P. Novák, F.-M. Petrat, and C. Veit, “Chemical vapor deposited silicon/graphite compound material as negative electrode for lithium-ion batteries.” *Electrochim. Solid-State Lett.*, **8**, A516 (2005).
- T. Schott, R. Robert, P. A. Ulmann, P. Lanz, S. Zürcher, M. E. Spahr, P. Novák, and S. Trabesinger, “Cycling behavior of silicon-containing graphite electrodes, part a: effect of the lithiation protocol.” *J. Phys. Chem. C*, **121**, 18423 (2017).
- M. Klett, J. A. Gilbert, K. Z. Pupek, S. E. Trask, and D. P. Abraham, “Layered oxide, graphite and silicon-graphite electrodes for lithium-ion cells: effect of electrolyte composition and cycling windows.” *J. Electrochim. Soc.*, **164**, A-6095 (2017).
- V. L. Chevrier, L. Liu, D.-B. Le, J. Lund, B. Molla, K. Reimer, L. J. Krause, L. D. Jensen, E. Figgemeier, and K. W. Eberman, “Evaluating Si-Based Materials for Li-Ion batteries in commercially relevant negative electrodes.” *J. Electrochim. Soc.*, **161**, A783 (2014).
- T. Schott, J. L. Gómez-Cámer, P. Novák, and S. Trabesinger, “Relationship between the Properties and Cycle Life of Si/C composites as performance-enhancing additives to graphite electrodes for Li-Ion batteries.” *J. Electrochim. Soc.*, **164**, A190 (2017).
- A. Trifonova, M. Winter, and J. O. Besenhard, “Structural and electrochemical characterization of tin-containing graphite compounds used as anodes for Li-ion batteries.” *J. Power Sources*, **174**, 800 (2007).
- Y. Surace, F. Jeschull, T. Schott, S. Zürcher, M. E. Spahr, and S. Trabesinger, “Improving the cycling stability of SnO₂-graphite electrodes.” *ACS Appl. Energy Mater.*, **2**, 7364 (2019).
- M. N. Obrovac and V. L. Chevrier, “Alloy negative electrodes for li-ion batteries.” *Chem. Rev.*, **114**, 11444 (2014).
- M. Otero, C. Heim, E. P. M. Leiva, N. Wagner, and A. Friedrich, “Design-considerations regarding Silicon/Graphite and Tin/Graphite composite electrodes for Lithium-Ion Batteries.” *Sci. Rep.*, **8**, 1 (2018).

11. A. Touidjine, M. Morcrette, M. Courty, C. Davoigne, M. Lejeune, N. Mariage, W. Porcher, and D. Larcher, "Partially oxidized silicon particles for stable aqueous slurries and practical Large-Scale Making of Si-Based Electrodes." *J. Electrochem. Soc.*, **162**, A1466 (2015).
12. M. N. Obrovac and L. J. Krause, "Reversible cycling of crystalline silicon powder." *J. Electrochem. Soc.*, **154**, A103 (2007).
13. F. Jeschull, J. Maibach, R. Félix, M. Wohlfahrt-Mehrens, K. Edström, M. Memm, and D. Brandell, "The solid electrolyte interphase (SEI) of water-processed graphite electrodes examined in a 65 mAh full cell configuration." *ACS Appl. Energy Mater.*, **1**, 5176 (2018).
14. F. Jeschull, D. Brandell, M. Wohlfahrt-Mehrens, and M. Memm, "Water-Soluble binders for Lithium-Ion battery graphite electrodes: slurry rheology, coating adhesion, and electrochemical performance." *Energy Technol.*, **5**, 2108 (2017).
15. F. Jeschull, Y. Surace, S. Zürcher, M. E. Spahr, P. Novák, and S. Trabesinger, "Electrochemistry and morphology of graphite negative electrodes containing silicon as capacity-enhancing electrode additive." *Electrochim. Acta*, **320**, 134602 (2019).
16. B. Philippe, R. Dedryvère, M. Gorgoi, H. Rensmo, D. Gonbeau, and K. Edström, "Role of the LiPF6Salt for the Long-Term Stability of silicon electrodes in Li-Ion Batteries—A photoelectron spectroscopy study." *Chem. Mater.*, **25**, 394 (2013).
17. B. Philippe, R. Dedryvère, M. Gorgoi, H. Rensmo, D. Gonbeau, and K. Edström, "Improved performance of nano-silicon electrodes using the salt LiFSI—A photoelectron spectroscopy study." *J. Am. Chem. Soc.*, **135**, 9829 (2013).
18. F. Lindgren, C. Xu, J. Maibach, A. M. Andersson, M. Marcinek, L. Niedzicki, T. Gustafsson, F. Björrefors, and K. Edström, "A hard X-ray photoelectron spectroscopy study on the solid electrolyte interphase of a lithium 4,5-dicyano-2-(trifluoromethyl)imidazolide based electrolyte for Si-electrodes." *J. Power Sources*, **301**, 105 (2016).
19. F. Jeschull, F. Lindgren, M. J. Lacey, F. Björrefors, K. Edström, and D. Brandell, "Influence of inactive electrode components on degradation phenomena in nano-Si electrodes for Li-ion batteries." *J. Power Sources*, **325**, 513 (2016).
20. C. R. Hernandez, A. Etienne, T. Douillard, D. Mazouzi, Z. Karkar, E. Maire, D. Guyomard, B. Lestriez, and L. Roué, "A Facile and very effective method to enhance the mechanical strength and the cyclability of Si-Based electrodes for Li-Ion batteries." *Adv. Energy Mater.*, **8**, 1701787 (2018).
21. B. P. N. Nguyen, J. Gaubicher, and B. Lestriez, "Analogy between electrochemical behaviour of thick silicon granular electrodes for lithium batteries and fine soils micromechanics." *Electrochim. Acta*, **120**, 319 (2014).
22. S. D. Beattie, D. Larcher, M. Morcrette, B. Simon, and J.-M. Tarascon, "Si electrodes for Li-Ion Batteries - a new way to look at an old problem." *J. Electrochem. Soc.*, **155**, A158 (2008).
23. Z. Du, R. A. Dunlap, and M. N. Obrovac, "High energy density calendered si alloy/graphite anodes." *J. Electrochem. Soc.*, **161**, A1698 (2014).
24. R. Jung, M. Metzger, D. Haering, S. Solchenbach, C. Marino, N. Tsiorvaras, C. Stinner, and H. A. Gasteiger, "Consumption of Fluoroethylene Carbonate (FEC) on Si-C Composite Electrodes for Li-Ion Batteries." *J. Electrochem. Soc.*, **163**, A1705 (2016).
25. D. Yoon, M. Marinaro, P. Axmann, and M. Wohlfahrt-Mehrens, "Communication —quantitative analysis of consumption of fluoroethylene carbonate additives on silicon alloy anodes." *J. Electrochem. Soc.*, **165**, A2467 (2018).
26. R. Petibon, V. L. Chevrier, C. P. Aiken, D. S. Hall, S. R. Hyatt, R. Shunmugam Sundaram, and J. R. Dahn, "Studies of the capacity fade mechanisms of LiCoO₂/Si-Alloy: graphite cells." *J. Electrochem. Soc.*, **163**, A1146 (2016).
27. W. Märkle, J. F. Colin, D. Goers, M. E. Spahr, and P. Novák, "In situ X-ray diffraction study of different graphites in a propylene carbonate based electrolyte at very positive potentials." *Electrochim. Acta*, **55**, 4964 (2010).
28. M. Winter, J. O. Besenhard, M. E. Spahr, and P. Novák, "Insertion Electrode Materials for Rechargeable Lithium Batteries." *Adv. Mater.*, **10**, 725 (1998).
29. H. Buqa, A. Würsig, J. Vetter, M. E. Spahr, F. Krumeich, and P. Novák, "SEI film formation on highly crystalline graphitic materials in lithium-ion batteries." *J. Power Sources*, **153**, 385 (2006).
30. H. Buqa, A. Würsig, D. Goers, L. J. Hardwick, M. Holzapfel, P. Novák, F. Krumeich, and M. E. Spahr, "Behaviour of highly crystalline graphites in lithium-ion cells with propylene carbonate containing electrolytes." *J. Power Sources*, **146**, 134 (2005).
31. M. Wetjen, D. Pritzl, R. Jung, S. Solchenbach, R. Ghadimi, and H. A. Gasteiger, "Differentiating the degradation phenomena in Silicon-Graphite electrodes for Lithium-ion batteries." *J. Electrochem. Soc.*, **164**, A2840 (2017).
32. H.-J. Peng, "Unravelling the cell ageing phenomena in aprotic Lithium-Nickel-Cobalt-Manganese-Oxide, ETH Zürich (2016), <https://www.research-collection.ethz.ch/handle/20.500.11850/122818>.
33. M. E. Spahr, D. Goers, A. Leone, S. Stallone, and E. Grivei, "Development of carbon conductive additives for advanced lithium ion batteries." *J. Power Sources*, **196**, 3404 (2011).
34. J. T. Dudley et al., "Conductivity of electrolytes for rechargeable lithium batteries." *J. Power Sources*, **35**, 59 (1991).
35. H. Zheng, R. Yang, G. Liu, X. Song, and V. S. Battaglia, "Cooperation between active material, polymeric binder and conductive carbon additive in lithium ion battery cathode." *J. Phys. Chem. C*, **116**, 4875 (2012).
36. E. Panabièvre, J.-C. Badot, O. Dubrunfaut, A. Etienne, and B. Lestriez, "Electronic and Ionic dynamics coupled at Solid-Liquid electrolyte interfaces in porous Nanocomposites of carbon black, Poly(vinylidene fluoride), and γ -Alumina." *J. Phys. Chem. C*, **121**, 8364 (2017).
37. M. Winter, P. Novák, and A. Monnier, "Graphites for Lithium-Ion cells: the correlation of the First-Cycle Charge Loss with the Brunauer–Emmett–Teller surface area." *J. Electrochem. Soc.*, **145**, 428 (1998).
38. J. L. Gómez-Cámer, C. Bünzli, M. M. Hantel, T. Poux, and P. Novák, "On the correlation between electrode expansion and cycling stability of graphite/Si electrodes for Li-ion batteries." *Carbon N. Y.*, **105**, 42 (2016).
39. S. J. An, J. Li, C. Daniel, H. M. Meyer, S. E. Trask, B. J. Polzin, and D. L. Wood III, "Electrolyte volume effects on electrochemical performance and solid electrolyte interphase in Si-Graphite/NMC Lithium-Ion pouch cells." *ACS Appl. Mater. Interfaces*, **9**, 18799 (2017).
40. S. Müller, J. Eller, M. Ebner, C. Burns, J. R. Dahn, and V. Wood, "Quantifying inhomogeneity of lithium ion battery electrodes and its influence on electrochemical performance." *J. Electrochem. Soc.*, **165**, A339 (2018).
41. J. Billaud, F. Bouville, T. Magrini, C. Villevieille, and A. R. Studart, "Magnetically aligned graphite electrodes for high-rate performance Li-ion batteries." *Nat. Energy*, **1**, 1 (2016).
42. W. B. Hawley and J. Li, "Electrode manufacturing for lithium-ion batteries—Analysis of current and next generation processing." *J. Energy Storage*, **25**, 100862 (2019).
43. M. Baunach, S. Jaiser, S. Schmelzle, H. Nirschl, P. Scharfer, and W. Schabel, "Delamination behavior of lithium-ion battery anodes: Influence of drying temperature during electrode processing." *Dry. Technol.*, **34**, 462 (2016).
44. S. Jaiser, M. Müller, M. Baunach, W. Bauer, P. Scharfer, and W. Schabel, "Investigations of film solidification and binder migration during drying of Li-Ion battery anodes." *J. Power Sources*, **318**, 210 (2016).
45. E. Lignee, B. Lestriez, and D. Guyomard, "Relationships between processing, morphology and discharge capacity of the composite electrode." *J. Power Sources*, **174**, 716 (2007).
46. K. A. Hays, R. E. Ruther, A. J. Kukay, P. Cao, T. Saito, D. L. Wood III, and J. Li, "What makes lithium substituted polyacrylic acid a better binder than polyacrylic acid for silicon-graphite composite anodes?" *J. Power Sources*, **384**, 136 (2018).
47. B. Koo, H. Kim, Y. Cho, K. T. Lee, N.-S. Choi, and J. Cho, "A highly cross-linked polymeric binder for high-performance silicon negative electrodes in lithium ion batteries." *Angew. Chem. Int. Ed.*, **51**, 8762 (2012).
48. A. Tranchot, H. Idrissi, P. X. Thivel, and L. Roué, "Impact of the Slurry pH on the Expansion/Contraction Behavior of Silicon/Carbon/Carboxymethylcellulose Electrodes for Li-Ion Batteries." *J. Electrochem. Soc.*, **163**, A1020 (2016).
49. A. Magasinski, B. Zdyrko, I. Kovalenko, B. Hertzberg, R. Burtovyy, of Huebner, T. F. Fuller, I. Luzinov, and G. Yushin, "Toward efficient binders for Li-ion battery Si-based anodes: polyacrylic acid." *ACS Appl. Mater. Interfaces*, **2**, 3004 (2010).
50. F. Jeschull, M. J. Lacey, and D. Brandell, "Functional binders as graphite exfoliation suppressants in aggressive electrolytes for lithium-ion batteries." *Electrochim. Acta*, **175**, 141 (2015).
51. N. Shpigel, M. D. Levi, S. Sigalov, O. Girshevitz, D. Aurbach, L. Daikhin, N. Jäckel, and V. Presser, "Non-Invasive In Situ Dynamic Monitoring of Elastic Properties of Composite Battery Electrodes by EQCM-D." *Angew. Chemie Int. Ed.*, **54**, 12353 (2015).
52. S. Komaba, N. Yabuuchi, T. Ozeki, K. Okushi, H. Yui, K. Konno, Y. Katayama, and T. Miura, "Functional binders for reversible lithium intercalation into graphite in propylene carbonate and ionic liquid media." *J. Power Sources*, **195**, 6069 (2010).
53. F. Jeschull, J. Maibach, K. Edström, and D. Brandell, "On the electrochemical properties and interphase composition of graphite: PVdF-HFP electrodes in dependence of binder content." *J. Electrochem. Soc.*, **164**, A1765 (2017).
54. W. Bauer, "Special features of powder technology for the production of lithium-ion batteries." *InterCeram.*, **68**, 18 (2019).
55. W. Bauer and D. Nötzel, "Rheological properties and stability of NMP based cathode slurries for lithium ion batteries." *Ceram. Int.*, **40**, 4591 (2014).
56. G. Liu, H. Zheng, A. S. Simens, A. M. Minor, X. Song, and V. S. Battaglia, "Optimization of acetylene black conductive additive and PVDF composition for High-Power rechargeable Lithium-Ion Cells." *J. Electrochem. Soc.*, **154**, A1129 (2007).
57. E. Lignee, B. Lestriez, O. Richard, and D. Guyomard, "Optimizing lithium battery performance from a tailor-made processing of the positive composite electrode." *J. Phys. Chem. Solids*, **67**, 1275 (2006).
58. N. Delpeuch, D. Mazouzi, N. Dupré, P. Moreau, M. Cerbelaud, J. S. Bridel, E. De Vito, D. Guyomard, B. Lestriez, and B. Humbert, "Critical role of silicon nanoparticles surface on lithium cell electrochemical performance analyzed by FTIR, Raman, EELS, XPS, NMR, and BDS spectroscopies." *J. Phys. Chem. C*, **118**, 17318 (2014).
59. Z. Karkar, D. Guyomard, L. Roué, and B. Lestriez, "A comparative study of polyacrylic acid (PAA) and carboxymethyl cellulose (CMC) binders for Si-based electrodes." *Electrochim. Acta*, **258**, 453 (2017).
60. F. Jeschull, F. Scott, and S. Trabesinger, "Interactions of silicon nanoparticles with carboxymethyl cellulose and carboxylic acids in negative electrodes of lithium-ion batteries." *J. Power Sources*, **431**, 63 (2019).
61. B. P. N. Nguyen, S. Chazelle, M. Cerbelaud, W. Porcher, and B. Lestriez, "Manufacturing of industry-relevant silicon negative composite electrodes for lithium ion-cells." *J. Power Sources*, **262**, 112 (2014).
62. T. Schott, R. Robert, S. Pacheco Benito, P. A. Ullmann, P. Lanz, S. Zürcher, M. E. Spahr, P. Novák, and S. Trabesinger, "Cycling behavior of Silicon-Containing Graphite electrodes, Part B: effect of the silicon source." *J. Phys. Chem. C*, **121**, 25718 (2017).
63. W. M. Dose, V. A. Maroni, M. J. Piernas-Muñoz, S. E. Trask, I. Bloom, and C. S. Johnson, "Assessment of Li-Inventory in Cycled Si-Graphite Anodes Using LiFePO₄ as a Diagnostic Cathode." *J. Electrochem. Soc.*, **165**, A2389 (2018).
64. T. Schott, J. L. Gómez-Cámer, C. Bünzli, P. Novák, and S. Trabesinger, "The counterintuitive impact of separator-electrolyte combinations on the cycle life of graphite–silicon composite electrodes." *J. Power Sources*, **343**, 142 (2017).

Supporting Information

Graphite Particle-Size Induced Morphological and Performance Changes of Graphite–Silicon Electrodes

Fabian Jeschull[†], Yuri Surace[†], Simone Zürcher[‡], Giacomo Lari[‡], Michael E. Spahr[‡], Petr Novák[†], Sigita Trabesinger^{†,*}

[†]Electrochemistry Laboratory, Forschungsstrasse 111, 5232 Villigen PSI, Switzerland

[‡]Imerys Graphite & Carbon, Via Cantonale 65, 6804 Bironico, Switzerland

*corresponding author: e-mail: sigita.trabesinger@psi.ch. Phone: +41 56 310 5775

1. Cycling of Si-free graphite electrodes

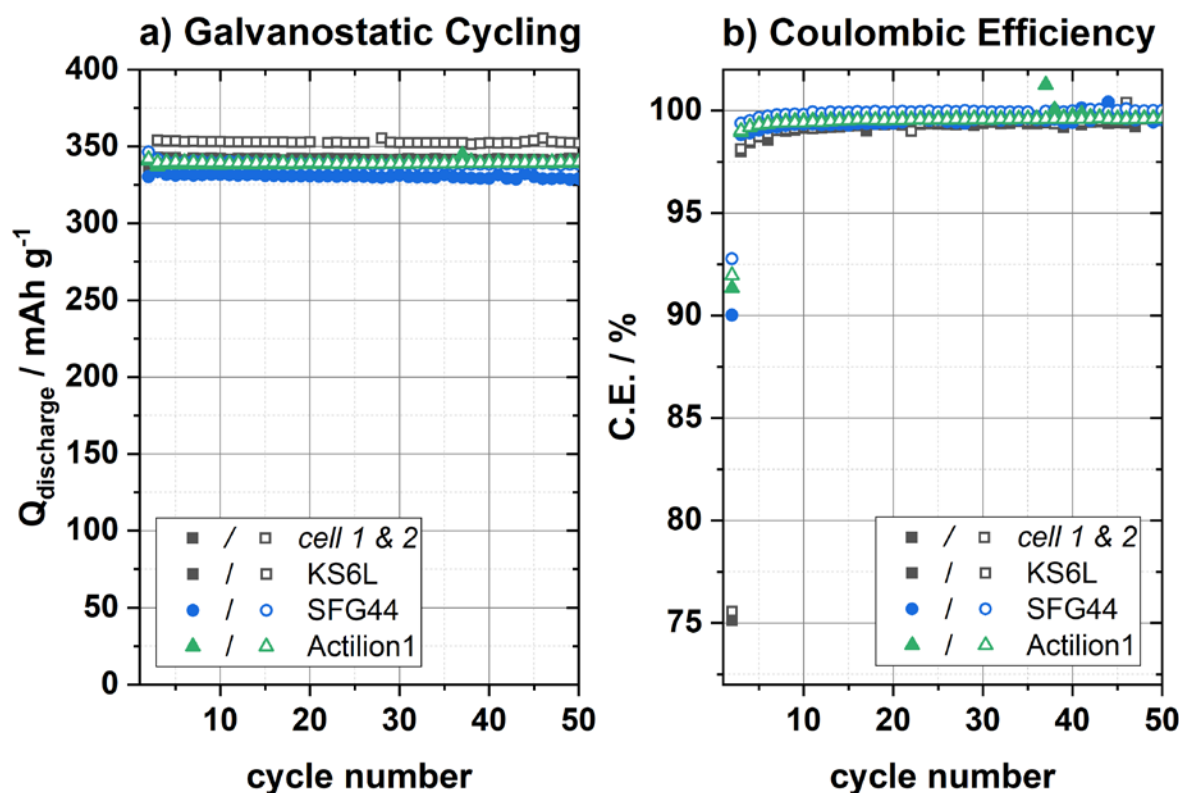


Figure S-1. Galvanostatic cycling (a) and corresponding Coulombic efficiency (b) for Si-free graphite electrode formulations comprising KS6L ($d_{90} < 6.5 \mu\text{m}$), SFG44 ($d_{90} < 48.4 \mu\text{m}$) and Actilion1 ($d_{90} < 28.8 \mu\text{m}$). Two cells of each formulation were cycled, indicated by filled (cell 1) and empty (cell 2) symbols.

2. Statistical Data on KS6L:Si (w/w = 90:5) electrodes

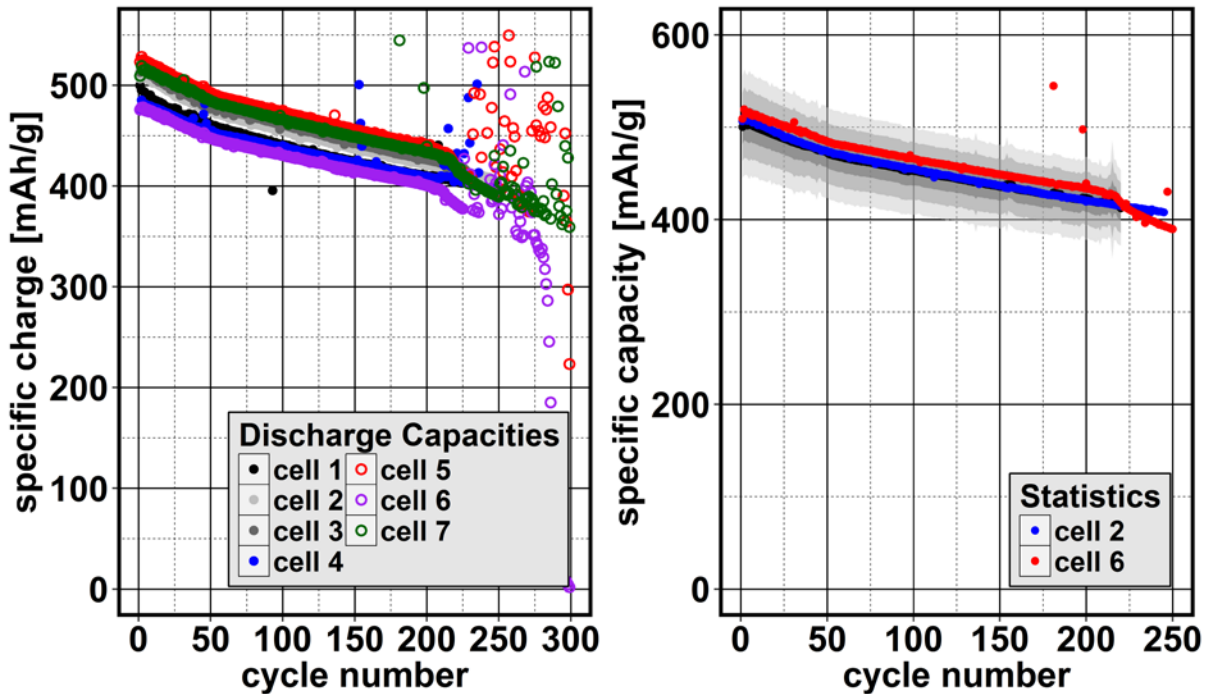


Figure S-2. Left panel: Galvanostatic cycling of 7 individual electrodes of the KS6L:Si (w/w = 90:5) formulation with 500 μ L electrolyte (LP30 + 4 wt.% FEC). Onset of cell failure is observed when the FEC additive is consumed. Right panel: Standard deviation out of the data shown in the left panel. The black line (beneath the blue one, cell 2) is the mean discharge capacity (Q_{mean}) of the data set. The grey areas indicate the standard deviation of the mean discharge capacity ($Q_{\text{mean}} \pm x\sigma$) with different widths for the standard deviation: $\pm 1\sigma$ (68.2%), $\pm 2\sigma$ (95.4%) and $\pm 3\sigma$ (99.7 %).

3. Comparison SFG44:Si (75:20) and SFG44:SFG6L:Si (67:8:20)

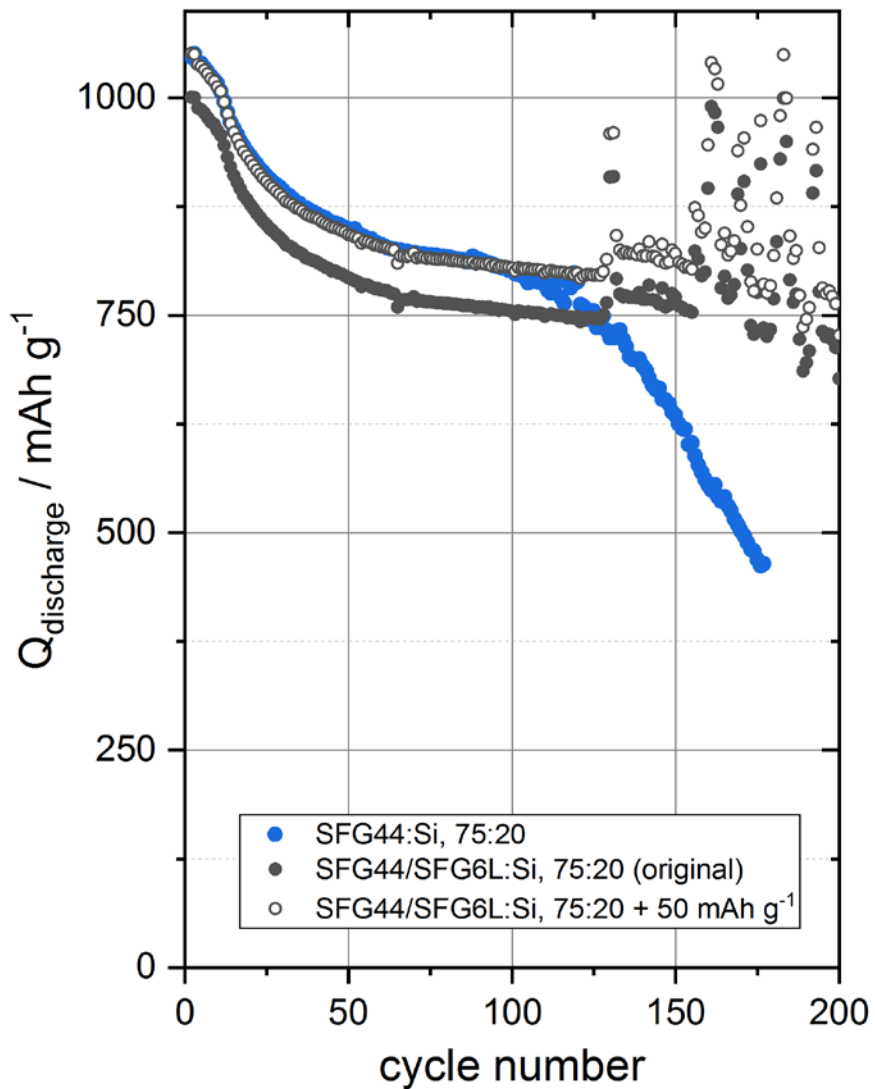
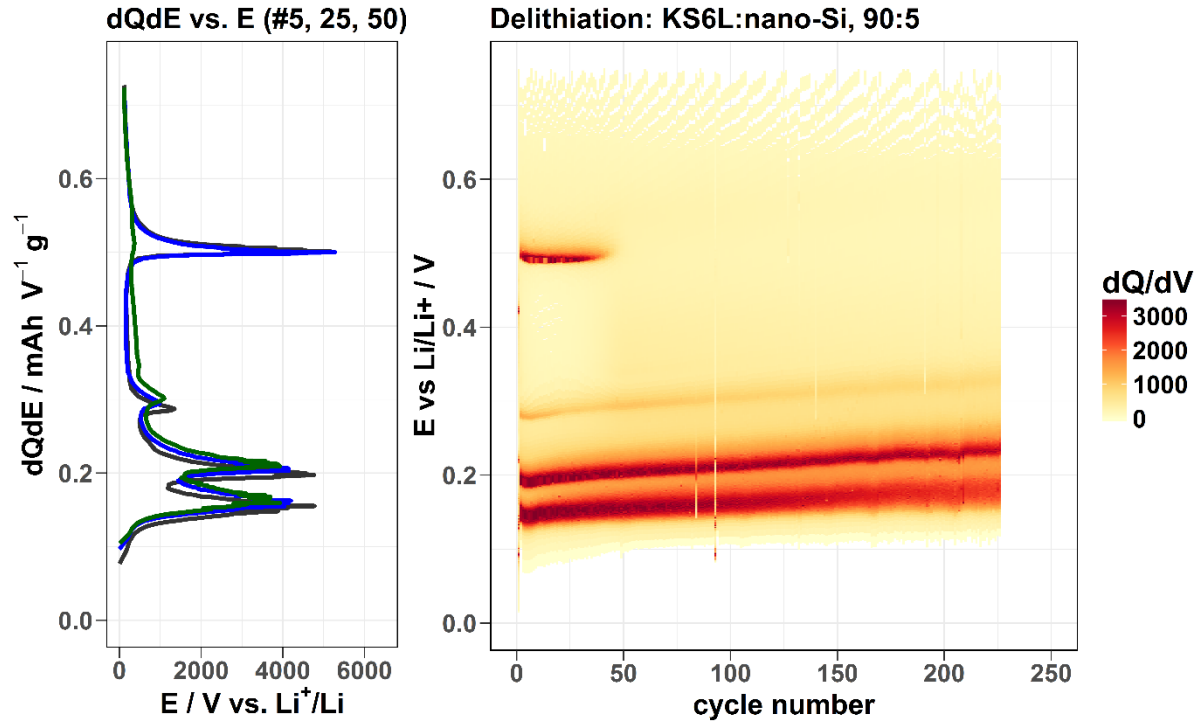


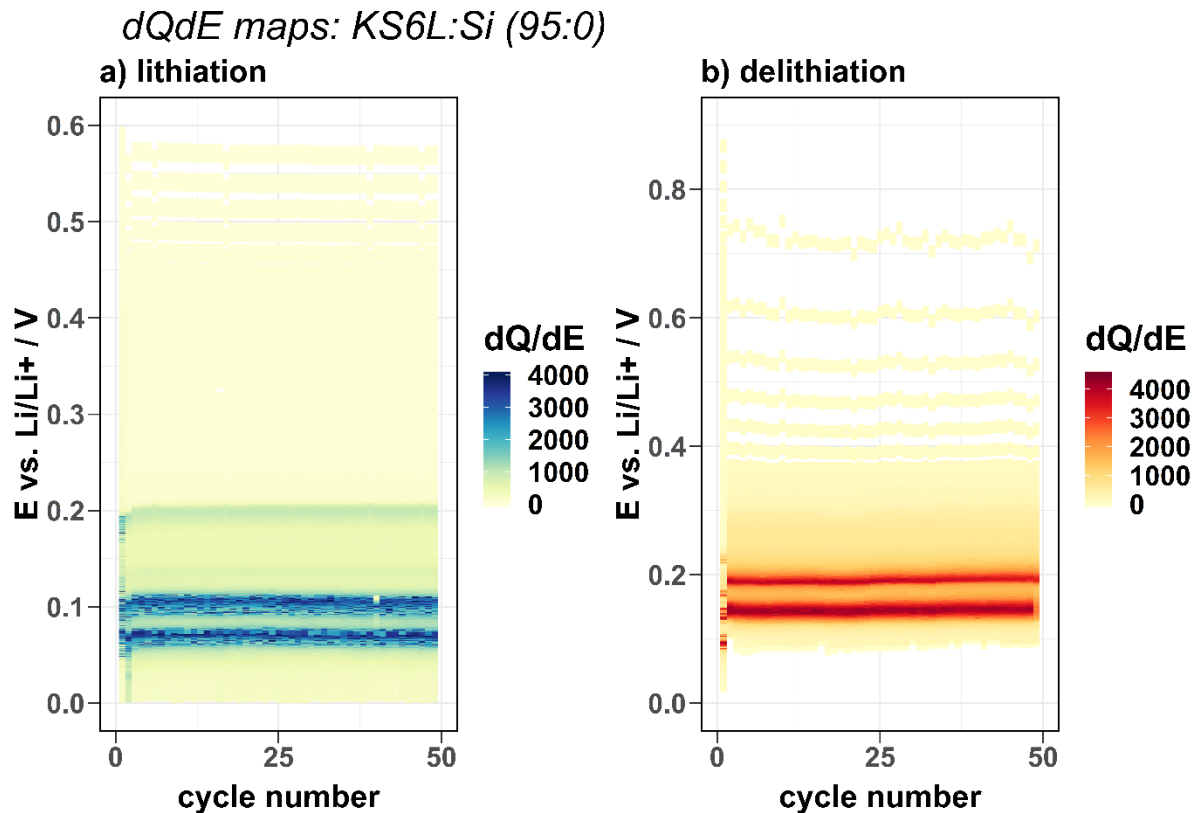
Figure S-3. Comparison of the capacity retention of a SFG44:Si composite (20 wt.% Si) and a corresponding SFG-blend (SFG44 + SFG6L, w/w = 8:1). The figure shows that the capacity fading is the same for both formulations, but the SFG44 composite (blue circles) has a higher initial discharge capacity. When the electrode comprising the SFG-blend is shifted by 50 mAh g⁻¹ up, the curves align, showing that both formulations indeed exhibit the same capacity fade and even the same fading features (such as the capacity drop after about 15 cycles).

4. Differential Capacity Plots

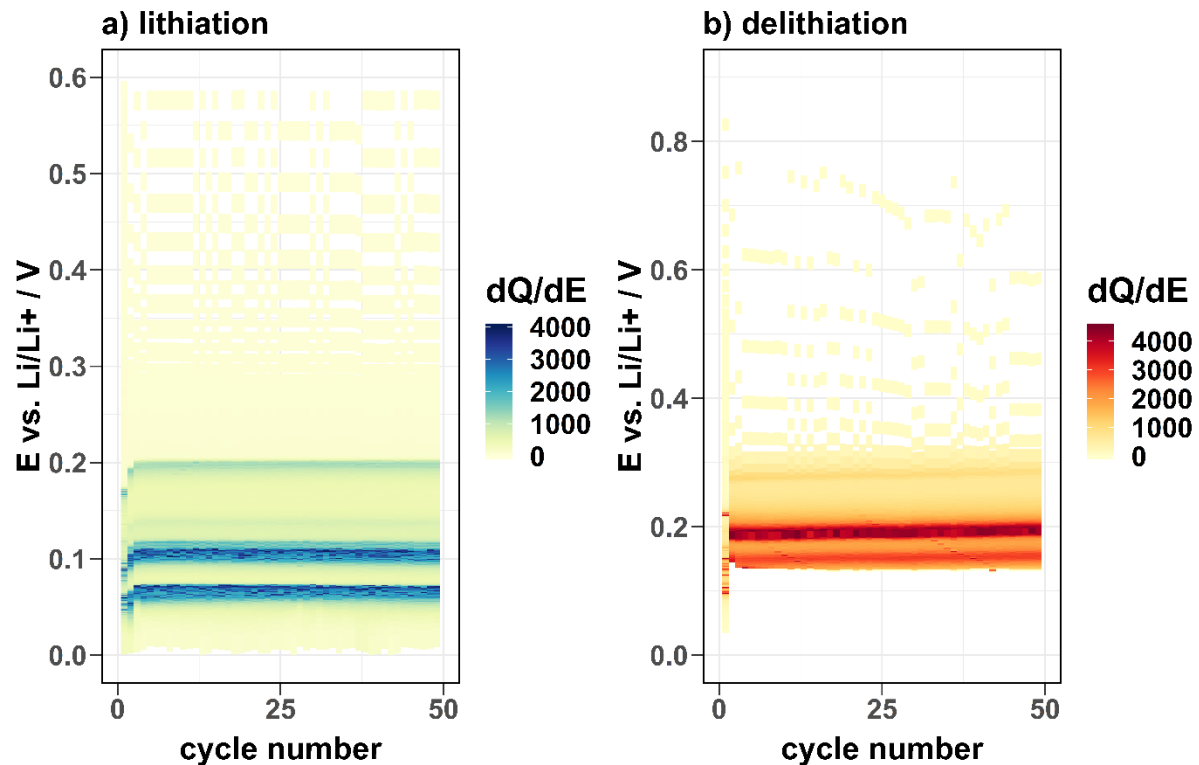
a) Example: Selected dQdE plots vs. dQdE maps



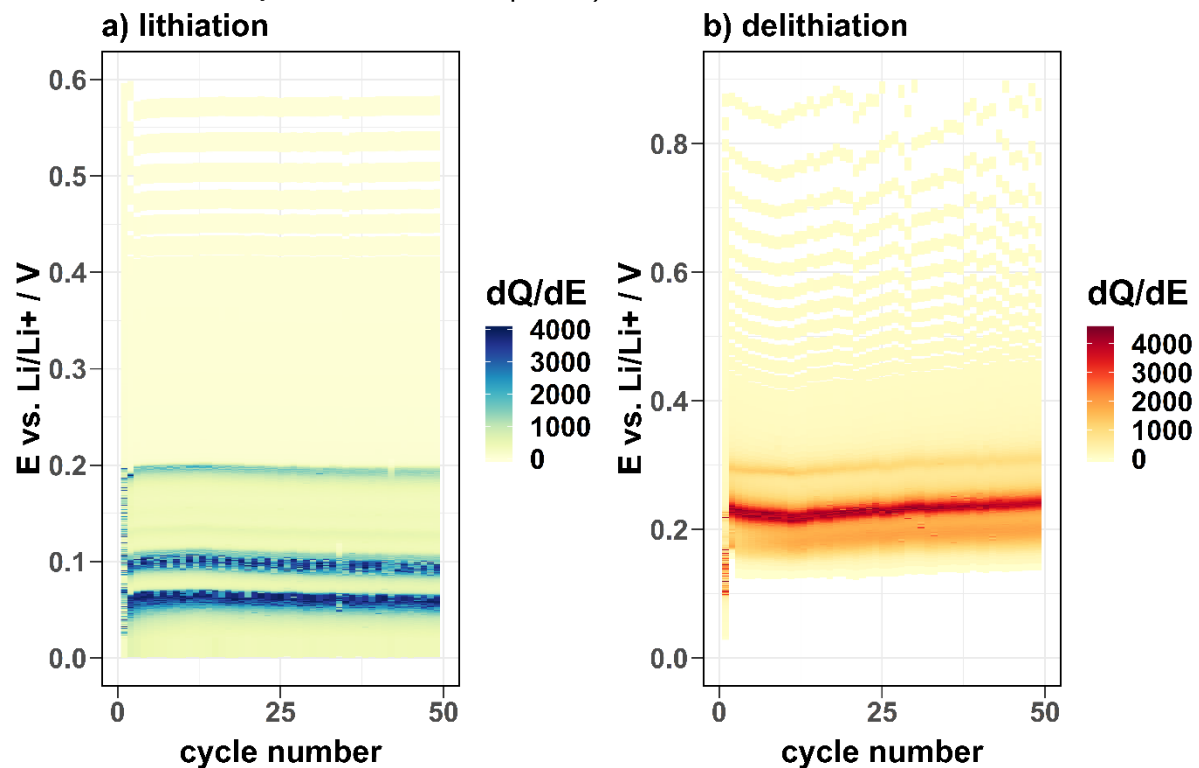
b) Si-free graphite Electrodes



dQdE maps: Actilion1:Si (95:0)



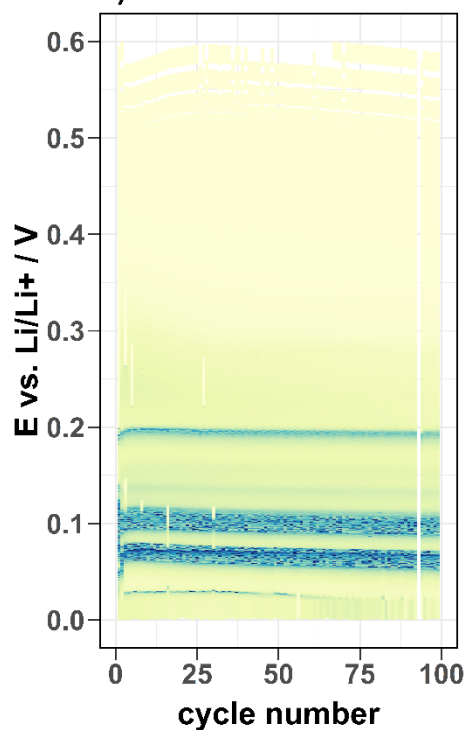
dQdE maps: SFG44:Si (95:0)



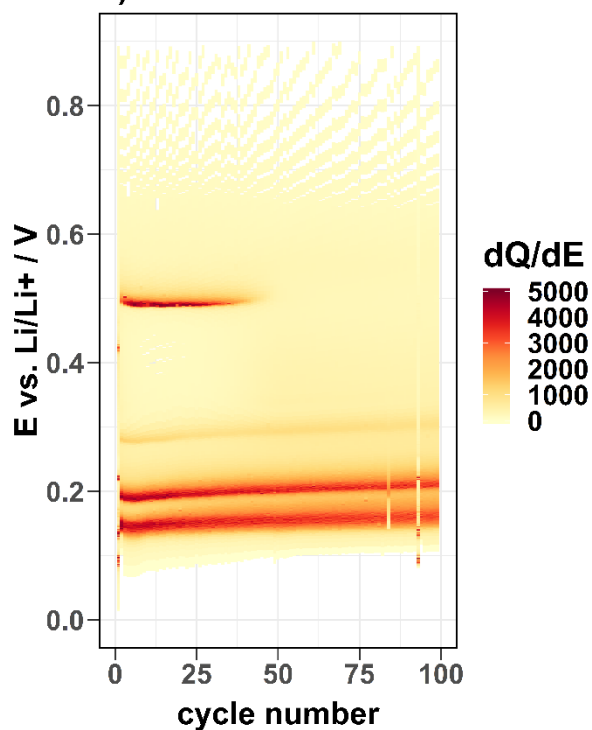
c) Graphite-Si blends with 5 wt.% Si

dQdE maps: KS6L:Si (90:5)

a) lithiation

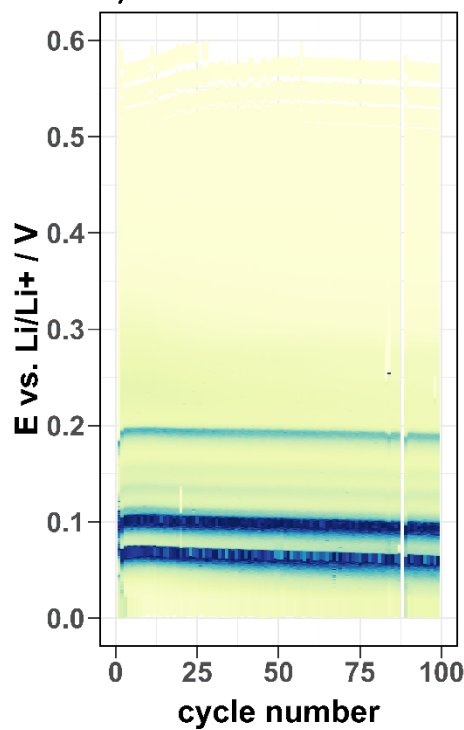


b) delithiation

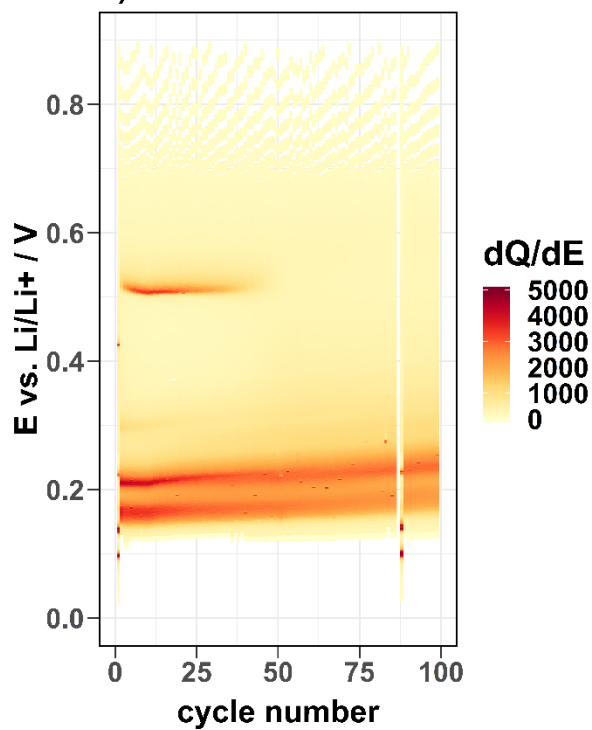


dQdE maps: SFG6L:Si (90:5)

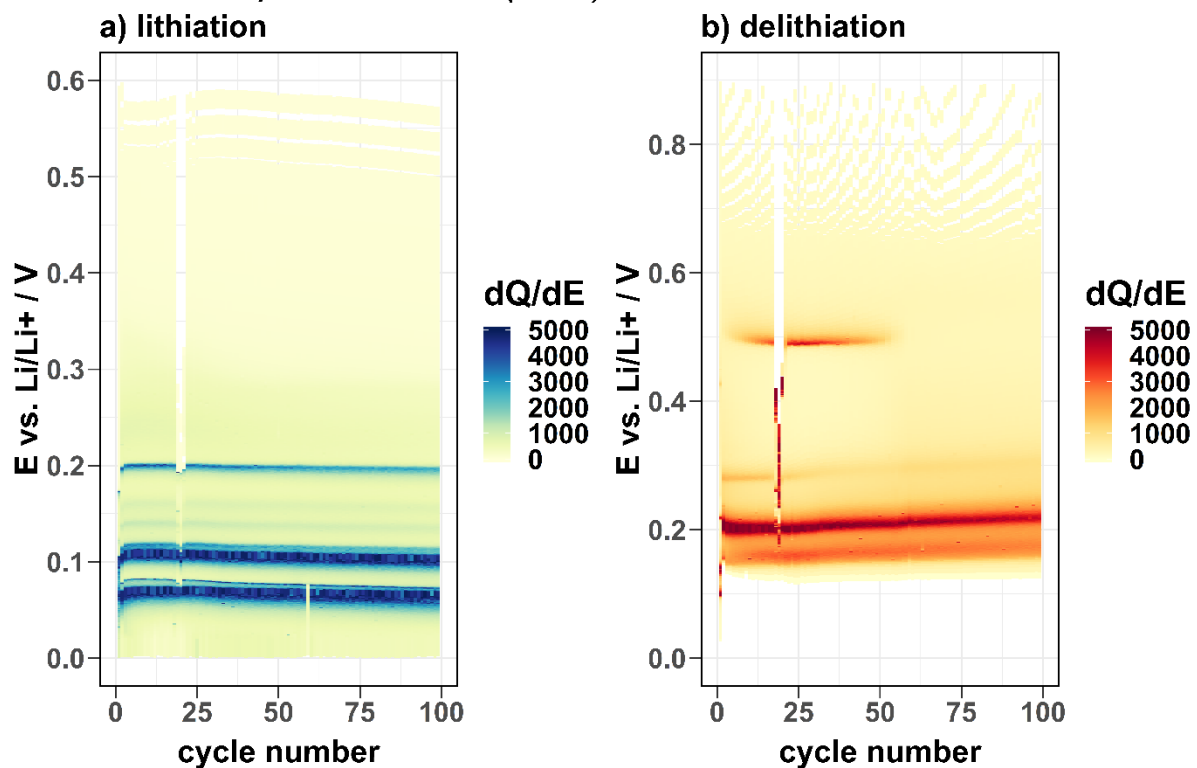
a) lithiation



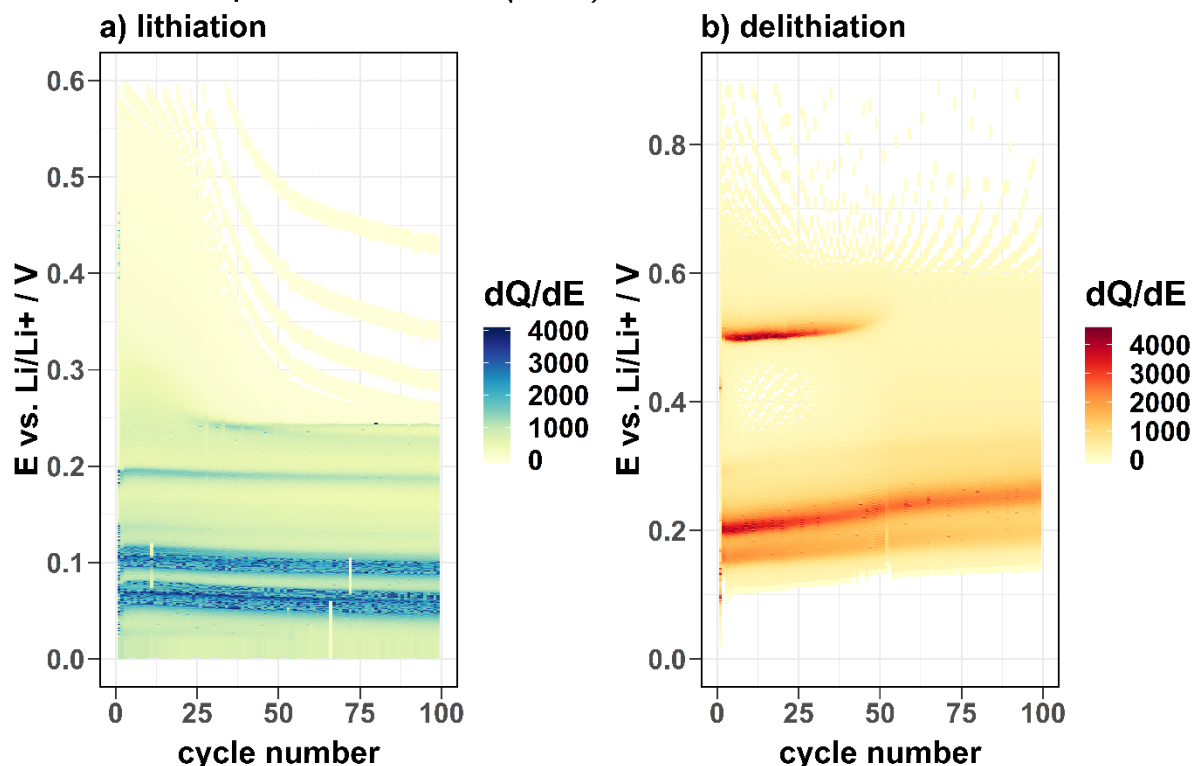
b) delithiation



dQdE maps: SFG44:Si (90:5)

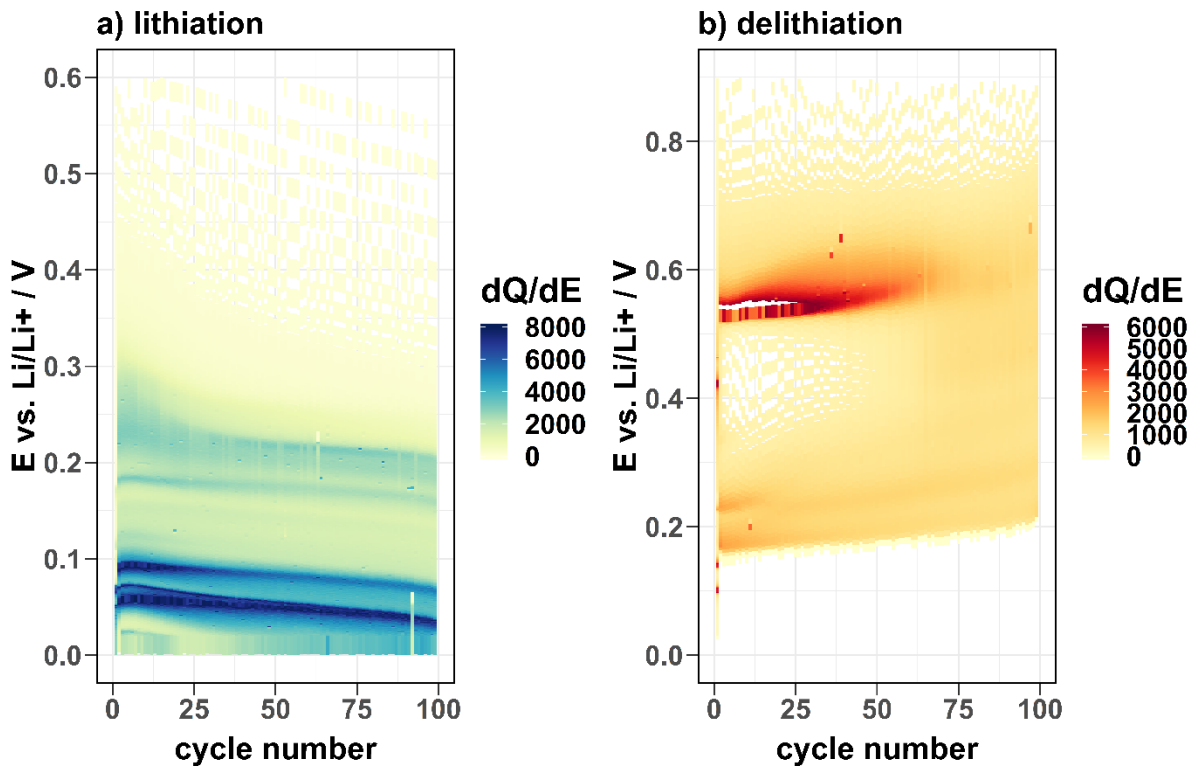


dQdE maps: Actilion1:Si (90:5)

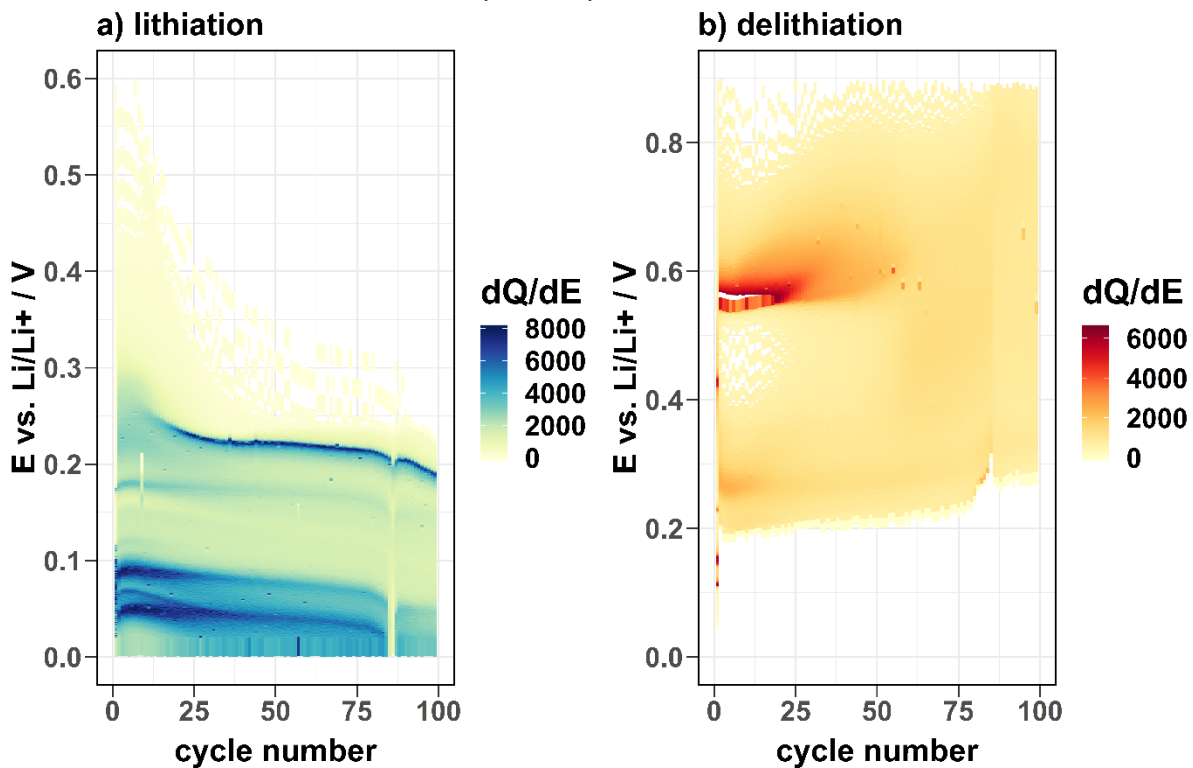


d) Graphite-Si blends with 20 wt.% Si

dQdE maps: KS6L:Si (75:20)



dQdE maps: SFG44:Si (75:20)



dQdE maps: Actilion1:Si (75:20)

